Nonlinear shear instabilities of alongshore currents on plane beaches

By J. S. ALLEN, P. A. NEWBERGER AND R. A. HOLMAN

College of Oceanic and Atmospheric Sciences, Oregon State University, Oceanography Admin Bldg 104, Corvallis, OR 97331-5503, USA

Evidence for the existence in the nearshore surf zone of energetic alongshore propagating waves with periods $O(100 \text{ s})$ and wavelengths $O(100 \text{ m})$ was found from observations by Oltman-Shay *et al.* (1989). These oscillations have wavelengths that are much too short to be surface gravity waves at the observed frequencies. The existence and properties of the wave-like motions were found to be related to the presence, strength and direction of an alongshore current in the surf zone. Based on a linear stability analysis of a mean alongshore current with offshore scale $O(100 \text{ m})$, Bowen & Holman (1989) described these fluctuations as unstable waves associated with a shear instability. Good agreement of wavelengths and wave speeds from observations and from predictions based on the most unstable linear mode was obtained by Dodd *et al.* (1992). The nonlinear dynamics of finite-amplitude shear instabilities of alongshore currents in the surf zone are studied here utilizing numerical experiments involving finite-difference solutions to the shallow water equations for idealized forced dissipative initial-value problems. Plane beach (i.e. constant slope) geometry is used with periodic boundary conditions in the alongshore direction. Forcing effects from obliquely incident breaking surface waves are approximated by an across-shore-varying steady force in the alongshore momentum equation. Dissipative effects are modelled by linear bottom friction. The solutions depend on the dimensionless parameter Q, which is the ratio of an advective to a frictional time scale. The steady frictionally balanced, forced, alongshore current is linearly unstable for Q less than a critical value Q_C. The response of the fluid is studied for different values of $\Delta Q = Q_C - Q$. In a set of experiments with the alongshore scale of the domain equal to the wavelength $2\pi/k_0$ of the most unstable linear mode, disturbances that propagate alongshore in the direction of the forced current with propagation velocities similar to the linear instability values are found for positive ΔQ. The disturbances equilibrate with constant amplitude for small ΔQ and with time-varying amplitudes for larger ΔQ. For increasing values of ΔQ the behaviour of this fluid system, as represented in a phase plane with area-averaged perturbation kinetic energy and area-averaged energy conversion as coordinates, is similar to that found in low-dimensional nonlinear dynamical systems including the existence of non-trivial steady solutions, bifurcation to a limit cycle, period-doubling bifurcations, and irregular chaotic oscillations. In experiments with the alongshore scale of the domain substantially larger than the wavelength of the most unstable linear mode, different behaviour is found. For small positive ΔQ, propagating disturbances grow at wavelength $2\pi/k_0$. If ΔQ is small enough, these waves equilibrate with constant or spatially varying amplitudes. For larger ΔQ, unstable waves of length $2\pi/k_0$ grow initially, but subsequently evolve into longer-wavelength nonlinear propagating steady or unsteady wave-like disturbances with behaviour dependent on ΔQ. The eventual development of large-scale nonlinear

propagating disturbances appears to be a robust feature of the flow response over plane beach geometry for moderate, positive values of ΔQ and indicates the possible existence in the nearshore surf zone of propagating finite-amplitude shear waves with properties not directly related to results of linear theory.

1. Introduction

Evidence for the existence in the nearshore surf zone of highly energetic alongshore propagating waves with periods $O(100 \text{ s})$ and wavelengths $O(100 \text{ m})$ was found from current measurements made as part of the SUPERDUCK experiment in October 1986 at Duck, NC by Oltman-Shay, Howd & Birkemeier (1989). These oscillations have alongshore wavelengths that are much too short to be surface gravity waves at the observed frequencies. The existence and properties of the wave-like motions are found to be related to the presence, strength and direction of an alongshore current in the surf zone. In particular, the waves exist only when an alongshore current is present and they propagate in the direction of the current at a velocity less than, but similar to, the maximum current velocity. The fluctuations are characterized by a linear relation between frequency and alongshore wavenumber typical of linear non-dispersive waves. Based on an inviscid linear stability analysis of an idealized alongshore current with offshore scale $O(100 \text{ m})$, Bowen & Holman (1989) attributed these fluctuations to unstable waves associated with a shear instability. Dodd, Oltman-Shay & Thornton (1992) obtained good agreement of wavelengths and wave speeds from observations and from theoretical predictions based on the most unstable mode from a linear stability analysis utilizing realistic estimates of mean currents and beach bottom topography and including bottom friction effects. Additional studies concerning the applicability of results from linear stability analysis to the problem have been reported by Dodd & Thornton (1990), Dodd (1994) and Falqués & Iranzo (1994). Some preliminary results on the finite-amplitude behaviour of these shear instabilities have been obtained by Dodd & Thornton (1992) using weakly nonlinear theory and by Falqués, Iranzo & Caballeria (1994) and Deigaard *et al.* (1994) using numerical model experiments.

Several obvious fluid mechanical questions remain unanswered. If the observed motions are related to a shear instability, why does the instability not grow so that the flow breaks down into vortices and loses wave-like properties? Why are the observed wavelike properties so robust and so similar to linear waves if the mechanism involves an instability? Does an equilibration mechanism exist that stabilizes these waves at finite-amplitude? What is the nature of the finite-amplitude nonlinear behaviour and how does it depend on the forcing, the frictional dissipative process, and the beach geometry? We attempt to answer some of these questions by pursuing a study utilizing numerical, finite-difference solutions to the shallow-water equations for idealized problems in simple geometry.

It is relevant to note that the observations of Oltman-Shay *et al.* (1989) are for conditions where the beach bottom topography is characterized by the presence of a sand bar parallel to the shore. It seems most sensible for initial model studies, however, to utilize the simplest possible relevant bottom topography which is provided by a plane beach of constant slope. We use plane beach topography here to investigate first the finite-amplitude instability processes in simple geometry. One consequence
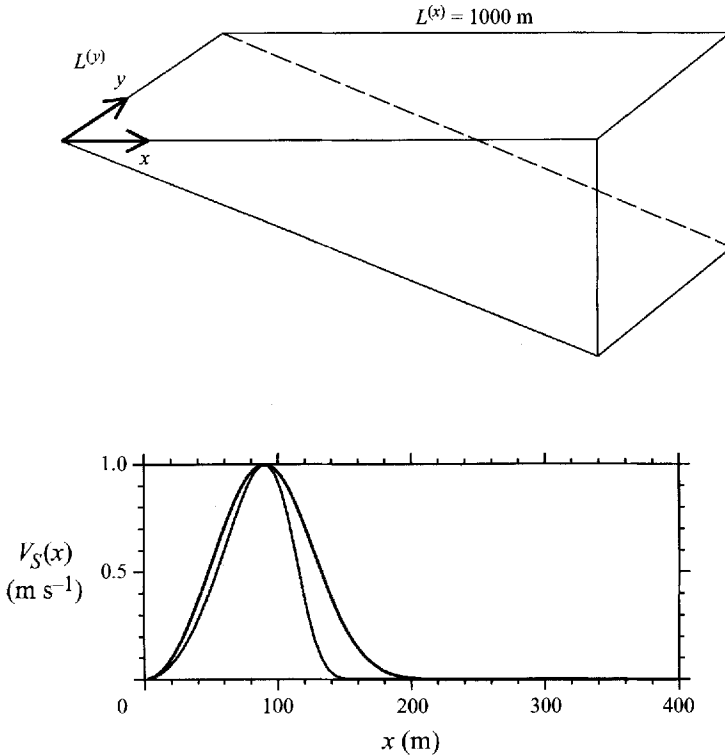
FIGURE 1. Schematic of model geometry showing the computational domain and the function $V_S(x)$ (2.13b) with $n = 3$ (heavy line) and with $n = 6$ (light line) used in the forcing (2.13a).

of this, however, is that restraint must be exercised in attempting direct, quantitative comparisons of model results with observations from the SUPERDUCK experiment.

The outline of the paper is as follows. The problem formulation is described in §2. Information from a linear stability analysis of alongshore currents relevant to the numerical experiments is included in §3. Results from three different sets of numerical experiments are presented in §§4, 5, and 6 and a summary is given in §7.

2. Formulation

Numerical experiments involving finite-difference solutions to the shallow-water equations for idealized forced dissipative initial-value problems are utilized to study the nonlinear dynamics associated with shear instabilities of alongshore currents in the surf zone. We deliberately select the simplest fluid dynamical system that retains the essential physics of this problem. Plane beach (i.e. constant slope) geometry, periodic in the alongshore direction and bounded offshore of the region of interest by a vertical wall, is utilized (see figure 1). Forcing effects from obliquely incident breaking surface waves are approximated by a steady body force in the alongshore momentum equation. Dissipation is modelled by linear bottom friction. Weak biharmonic friction is also included to provide additional dissipation at high wavenumbers in the numerical finite-difference solutions. The rigid-lid approximation, discussed further below, is also invoked.

The governing equations are

$$(hu)_x + (hv)_y = 0, \qquad (2.1a)$$

$$u_t + uu_x + vu_y = -p_x/\rho_0 - \mu u/h - \nu\nabla^4 u, \tag{2.1b}$$

$$v_t + uv_x + vv_y = -p_y/\rho_0 - \mu[v - V]/h - \nu\nabla^4 v, \tag{2.1c}$$

where Cartesian coordinates (x, y) are aligned across-shore and alongshore, respectively, with $x = 0$ at the coast, t is time, (u, v) are velocity components in the (x, y) directions, p is pressure, ρ_0 is the constant fluid density, $h = h(x)$ is the depth, μ is a bottom friction coefficient, and ν is a biharmonic diffusion coefficient. The applied body force per unit volume in (2.1c) has been expressed as $\mathcal{F} = \rho_0\mu V(x, y)/h$, so that with $V = V_S(x)$ and $\nu = 0$ the steady, forced, frictionally balanced currents are $v = V_S(x)$, $u = 0$. Subscripts (x, y, t) denote partial differentiation.

Dimensionless variables are formed using the characteristic scales (L, h_0, V_{SM}) for, respectively, a horizontal length scale, a depth scale, and a velocity. The characteristic time scale $t_C = L/V_{SM}$. The characteristic velocity V_{SM} is related to the magnitude of the forcing based on scaling appropriate for a steady, y-independent, forced flow balanced by bottom friction and is chosen equal to the maximum absolute value of $V_S(x)$. It is natural to choose the characteristic horizontal length scale L as the across-shore distance from the coast to the x position where $V_S(x = L) = V_{SM}$ and the characteristic depth as $h_0 = h(x = L)$. With dimensionless variables denoted by stars, we have

$$(x, y) = (x^\star, y^\star)L, \quad t = t^\star L/V_{SM}, \quad h = h^\star h_0, \tag{2.2a–c}$$

$$(u, v) = (u^\star, v^\star)V_{SM}, \quad p = p^\star\rho_0 V_{SM}^2, \quad V = V^\star V_{SM}. \tag{2.2d–f}$$

The equations (2.1) in dimensionless variables (dropping the stars) are

$$(hu)_x + (hv)_y = 0, \tag{2.3a}$$

$$u_t + uu_x + vu_y = -p_x - Qu/h - R^{-1}\nabla^4 u, \tag{2.3b}$$

$$v_t + uv_x + vv_y = -p_y - Q[v - V]/h - R^{-1}\nabla^4 v, \tag{2.3c}$$

where

$$Q = \mu L/(V_{SM}h_0), \tag{2.4}$$

$$R^{-1} = \nu/(V_{SM}L^3). \tag{2.5}$$

In general, we consider

$$R^{-1} \ll 1, \tag{2.6}$$

so that Q is the primary dimensionless parameter upon which the solutions depend. Note that Q represents the ratio of an advective time scale L/V_{SM} to a bottom friction time scale h_0/μ. For a plane beach, the ratio h_0/L in Q is the beach slope.

The rigid-lid approximation is utilized based on the assumption that the characteristic time scale is the advective scale $t_C = L/V_{SM}$ and on the scaling estimate that

$$V_{SM}^2 \ll gh_0, \tag{2.7}$$

where g is the acceleration due to gravity (e.g. Bowen & Holman 1989; Dodd & Thornton 1990). The condition (2.7) is reasonably well satisfied for alongshore currents in the surf zone where typical scale values are $V_{SM} \approx 1$ m s^{-1} and $h_0 \simeq 3 - 5$ m.

The numerical experiments reported here are performed using dimensional variables. The dynamical similarity indicated by the dimensionless equations (2.3) and the dependence on the dimensionless parameters Q and R^{-1} can be recovered, of course, by rescaling (Appendix A). Henceforth, we use (2.1) and dimensional variables.

We note from (2.1*a*) that a transport streamfunction ψ may be defined such that

$$hu = -\psi_y, \quad hv = \psi_x. \qquad (2.8a,b)$$

In addition, an equation for the potential vorticity q, where

$$q = \zeta/h, \quad \zeta = v_x - u_y, \qquad (2.9a,b)$$

and where ζ is the vertical component of the vorticity, may be derived from (2.1):

$$q_t + uq_x + vq_y = (\mu/h)(V/h)_x - (\mu/h)[(v/h)_x - (u/h)_y] - (v/h)\nabla^4\zeta. \qquad (2.10)$$

In the absence of forcing ($V = 0$) and friction ($\mu = v = 0$), (2.10) reduces to

$$q_t + uq_x + vq_y = 0, \qquad (2.11)$$

which implies that q is conserved on fluid particles.

The equations (2.1*a,b,c*) are solved numerically using finite-difference approximations. The numerical methods are discussed in Appendix B. The geometry for the numerical experiments is shown in figure 1. The (x, y) dimensions of the domain are $(L^{(x)}, L^{(y)})$. The flow is assumed to be periodic in the alongshore direction y with period $L^{(y)}$. The boundary conditions in x correspond to no-normal flow

$$u = 0 \quad \text{at} \quad x = 0, L^{(x)}, \qquad (2.12a)$$

and to free-slip for the biharmonic momentum diffusion,

$$u_{xx} = v_x = v_{xxx} = 0 \quad \text{at} \quad x = 0, L^{(x)}. \qquad (2.12b)$$

We choose $L^{(x)}$ large enough so that the behaviour of the flow is not influenced by the finite domain size in x. For the numerical experiments reported here, we fix $L^{(x)} = 1000$ m and $h = 0.05x$. For the forcing, we assume

$$V(x, y) = V_S(x)\big(1 + \epsilon b(y)\big), \qquad (2.13a)$$

with

$$V_S(x) = C_0 x^2 \exp[-(x/\alpha)^n], \qquad (2.13b)$$

where $n = 3$ or $n = 6$. The constants C_0 and α are chosen so that the maximum magnitude of V_S is $V_{SM} = 1$ m s^{-1} at $x = L = 90$ m (figure 1). As a result, $h(x = L) = h_0 = 4.5$ m. The function

$$\epsilon b(y) = \epsilon \sum_{j=1}^{J} b_j \cos(2\pi jy/L^{(y)}), \qquad (2.13c)$$

where $\epsilon \ll 1$, is added to the forcing in some experiments to provide weak perturbations at alongshore wavenumbers $2\pi j/L^{(y)}, j = 1, ..., J$. The alongshore scale of the domain $L^{(y)}$ is chosen to be equal to a multiple of the wave length $2\pi/k_0$ of the most unstable linear mode for the basic flow $v = V_S(x)$ (§3), i.e.

$$L^{(y)} = m(2\pi/k_0), \qquad (2.14)$$

where m is an integer $m \geqslant 1$. We also fix $v = 10$ m^4 s^{-1}, so that $R^{-1} = 1.37 \times 10^{-5}$.

The magnitude of the bottom friction coefficient μ is varied over a range applicable to oceanographic conditions (e.g. Dodd *et al.* 1992; Dodd 1994) in different experiments with fixed values for $V_S(x)$ and $L^{(y)}$. With the other parameters held constant, $Q = \mu L/(V_{SM}h_0) = 20\mu$ and the variation of μ (m s^{-1}) may be interpreted in terms of the variation of the dimensionless parameter Q (Appendix A). The forcing $V_S(x)$

(2.13b) is chosen to satisfy $V_S(x \to \infty) \sim 0$ and $V_S(x = 0) = 0$ (with V_{Sx}/h finite at $x = 0$) and to have a single maximum value. Although the functional form of $V_S(x)$ shown in figure 1 is fixed by (2.13b), we emphasize that the particular values chosen for the maximum value V_{SM}, the offshore scale L, and the beach slope h_0/L are not binding since these values may be changed and interpreted also as variations in the dimensionless parameter Q (Appendix A).

For analysis of the results of the numerical experiments, it is useful to define an alongshore average and an area average as follows:

$$\bar{v} = \frac{1}{L^{(y)}} \int_0^{L^{(y)}} v \, \mathrm{d}y, \qquad \{\bar{v}\} = \frac{1}{L^{(x)}} \int_0^{L^{(x)}} \bar{v} \, \mathrm{d}x, \qquad (2.15a,b)$$

and to decompose the velocity field such that

$$v = \bar{v} + v', \quad u = u', \qquad (2.16a,b)$$

where, with $h = h(x)$ and periodicity in y, (2.1a) implies $\bar{u} = 0$.

The area-averaged equations for the energy in the alongshore-averaged flow and for the energy in the perturbations about the alongshore average derived from (2.1) with (2.15) and (2.16) are

$$\{\tfrac{1}{2}h\bar{v}^2\}_t = \{(h\overline{u'v'})\bar{v}_x\} + \mu\{V_S\bar{v}\} - \mu\{\bar{v}^2\} - \nu\{h\bar{v}\nabla^4\bar{v}\}, \qquad (2.17)$$

$$\{\tfrac{1}{2}h\overline{(u'^2 + v'^2)}\}_t = -\{(h\overline{u'v'})\bar{v}_x\} + \mu\{\overline{V'v'}\} - \mu\{\overline{u'^2 + v'^2}\} - \nu\{h\overline{(u'\nabla^4 u' + v'\nabla^4 v')}\}. \quad (2.18)$$

It is clear from (2.17) and (2.18) that the term

$$EC = -\{(h\overline{u'v'})\bar{v}_x\}, \qquad (2.19)$$

represents energy conversion from the alongshore-averaged flow to the perturbations. The potential vorticity q may likewise be decomposed:

$$q = \bar{q} + q', \quad \bar{q} = \bar{\zeta}/h, \quad q' = \zeta'/h, \qquad (2.20a\text{–}c)$$

where

$$\bar{\zeta} = \bar{v}_x, \quad \zeta' = v'_x - u'_y. \qquad (2.20d,e)$$

Equations for $\bar{q}$ and q' follow from (2.10):

$$\bar{q}_t + (h\overline{u'q'})_x/h + (\mu/h)\big[(\bar{v} - V_S)/h\big]_x + (\nu/h)\nabla^4\bar{\zeta} = 0, \qquad (2.21)$$

$$q'_t + u'\bar{q}_x + \bar{v}q'_y + u'q'_x + v'q'_y - (h\overline{u'q'})_x/h$$

$$+ (\mu/h)\big[(v'/h)_x - (V'/h)_x - (u'/h)_y\big] + (\nu/h)\nabla^4\zeta' = 0, \qquad (2.22)$$

where

$$\overline{u'q'_x} + \overline{v'q'_y} = \overline{(u'v'_x)}/h = (h\overline{u'q'})_x/h. \qquad (2.23)$$

For flows with $R^{-1} \ll 1$ that evolve such that $\bar{q}_t \simeq 0$, (2.21) reduces to

$$(h\overline{u'q'})_x \simeq -\mu\big[(\bar{v} - V_S)/h\big]_x, \qquad (2.24)$$

which implies that departures of $\bar{v}$ from V_S are forced by the alongshore-averaged across-shore flux of perturbation potential vorticity.

3. Linear stability

The linear stability of the basic alongshore current $v = V_S(x)$ is determined by standard procedures (e.g. Drazin & Reid 1981). For simplicity we assume here, based on (2.6), that $v = 0$. The variables are expressed as

$$u = \tilde{u}, \quad v = V_S + \tilde{v}, \quad p = \tilde{p}, \quad h\tilde{u} = -\tilde{\psi}_y, \quad h\tilde{v} = \tilde{\psi}_x, \qquad (3.1a\text{–}e)$$

$$\zeta_S = V_{Sx}, \quad q_S = \zeta_S/h, \quad \tilde{\zeta} = \tilde{v}_x - \tilde{u}_y, \quad \tilde{q} = \tilde{\zeta}/h. \qquad (3.1f,g)$$

Substituting (3.1) in (2.10) and retaining linear terms, we obtain

$$\tilde{q}_t + V_S\tilde{q}_y + \tilde{u}q_{Sx} = -(\mu/h)[(\tilde{v}/h)_x - (\tilde{u}/h)_y], \qquad (3.2)$$

which provides a single equation for the perturbation streamfunction $\tilde{\psi}$. We consider solutions of (3.2) of the form

$$\tilde{\psi} = \mathrm{Re}\{\phi(x)\exp[\mathrm{i}k(y - ct)]\}, \qquad (3.3)$$

where ϕ and c may be complex ($c = c_r + \mathrm{i}c_i$) and where Re denotes the real part. The resulting equation for ϕ is

$$\left(V_S - c - \mathrm{i}\frac{\mu}{kh}\right)\left(\phi_{xx} - \frac{h_x}{h}\phi_x - k^2\phi\right) - h\left(\frac{V_{Sx}}{h}\right)_x\phi + \mathrm{i}\frac{\mu}{kh^2}h_x\phi_x = 0. \qquad (3.4a)$$

The boundary conditions for (3.4a) follow from (2.12a) and are

$$\phi = 0 \quad \text{at} \quad x = 0, L^{(x)}. \qquad (3.4b)$$

The linear stability problem in this context for alongshore currents in the surf zone was first formulated for frictionless flow by Bowen & Holman (1989) with subsequent further analysis by Dodd & Thornton (1990). Characteristics of solutions to the linear stability problem with friction (3.4) using estimates of observed ocean currents for V_S and of corresponding beach bottom topography for h have been discussed and compared to observations by Dodd *et al.* (1992). Additional study of the applicability of linear stability analysis to the interpretation of oceanic observations is presented in Dodd (1994).

Solutions to (3.4) are obtained numerically using finite-difference approximations as explained in Appendix B. The basic flow $V_S(x)$ is given by (2.13b) with $n = 3$ or $n = 6$ (figure 1). These two functional forms for V are utilized as forcing functions in the numerical experiments.

Results of the linear stability calculations in terms of growth rate kc_i for the most unstable linear mode as a function of alongshore wavenumber k for different values of μ are shown in figure 2. The propagation velocity c_r as a function of k for $\mu = 0$ is also shown. For V_S with $n = 3$, we find in the frictionless limit $\mu = 0$ that the wavelength of the most unstable linear mode is approximately $2\pi/k_0 = 450$ m, with a growth rate of about 0.00139 s^{-1}, which converts to a growth time scale of 12 min. The corresponding propagation velocity $c_r = 0.65$ m s^{-1} which gives a period of $2\pi/(k_0c_r) = 11.5$ min. As μ is increased, the maximum growth rate decreases and the wavelength $2\pi/k_0$ of the most unstable mode decreases slightly. The propagation velocities c_r change little from the $\mu = 0$ values. For $\mu \geqslant \mu_C = 0.0095$ (corresponding to $Q_C = 0.19$), the flow is linearly stable.

Compared to V_S with $n = 3$, the velocity profile $V_S(x)$ with $n = 6$ has a substantially sharper fall-off in the offshore direction from the maximum at $x = 90$ m (figure 1). With $n = 6$, the resulting wavelength of the most unstable mode for $\mu = 0$ is 180 m,
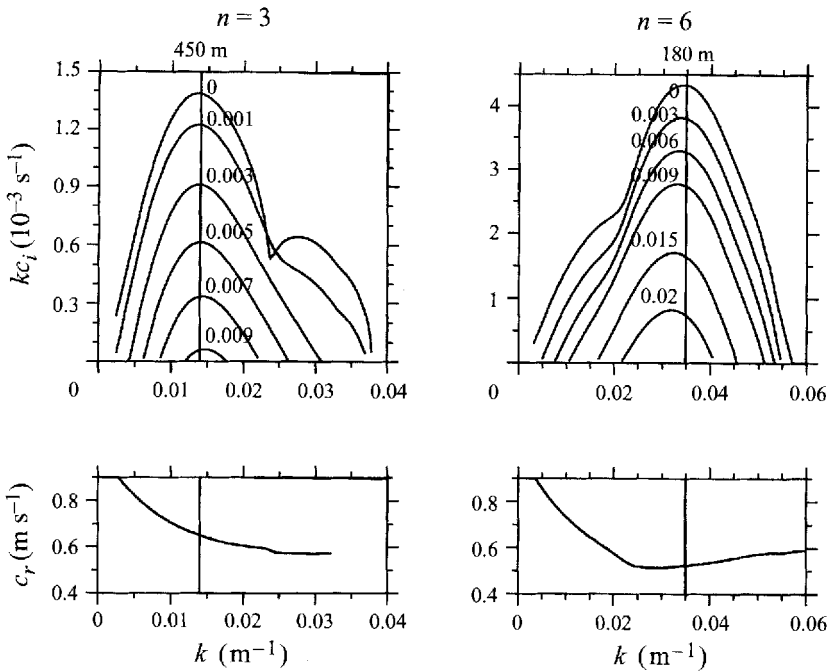
FIGURE 2. Results of linear stability calculations for the basic flow $v = V_S(x)$ with $n = 3$ and with $n = 6$ in terms of growth rate kc_i versus alongshore wavenumber k for different values of μ (m s^{-1}). Also shown is the propagation velocity c_r versus k for $\mu = 0$.

considerably shorter than the 450 m found with $n = 3$. The growth rate kc_i is 0.0043 s^{-1}, which is larger than with $n = 3$ and which gives a growth time scale of 3.9 min. The corresponding $c_r = 0.52$ m s^{-1} and period $2\pi/(k_0 c_r) = 5.8$ min. The tendency for larger growth rates to result as the gradient in $V_S(x)$ offshore of the maximum is increased was noted in the initial studies of Bowen & Holman (1989). As μ increases, the maximum growth rate decreases and, in this case, the corresponding wavelength $2\pi/k_0$ increases slightly. Again, the values of c_r remain similar to the $\mu = 0$ case. For $\mu \geqslant \mu_C = 0.0248(Q_C = 0.50)$ the flow is linearly stable.

4. Numerical experiments, $n = 3$, $m = 1$

In the first set of experiments, we utilize forcing (2.13) with the $n = 3$ profile for $V_S(x)$ and with $\epsilon = 0$. The domain length in the alongshore direction is equal to the wavelength of the most unstable linear mode with $\mu = 0$, i.e. $m = 1$ in (2.14) so that $L^{(y)} = 2\pi/k_0 = 450$ m. The magnitude of the bottom friction coefficient μ is varied while all other parameters are held constant as described in §2. The initial conditions consist of v equal to the steady, frictionally balanced flow $V_S(x)$, plus small perturbations in u and v proportional to the most unstable linear mode at the corresponding value of μ and $2\pi/k = 450$ m and scaled so that the maximum perturbation in $(u^2 + v^2)^{1/2}$ is 0.01 m s^{-1}.

Time series of the across-shore velocity u at $x = 90$ m, $y = \frac{1}{4}L^{(y)} = 112.5$ m from a set of experiments with different values of μ are plotted in figure 3. For $\mu = 0.01$, the profile $V_S(x)$ is stable (figure 2) and we find $u = 0$. As μ is decreased to $\mu = 0.0075$ so that the basic flow is weakly unstable, regular oscillations in u are found with nearly constant amplitude for $t > 10$ h and with a period of about 13.3 min. These
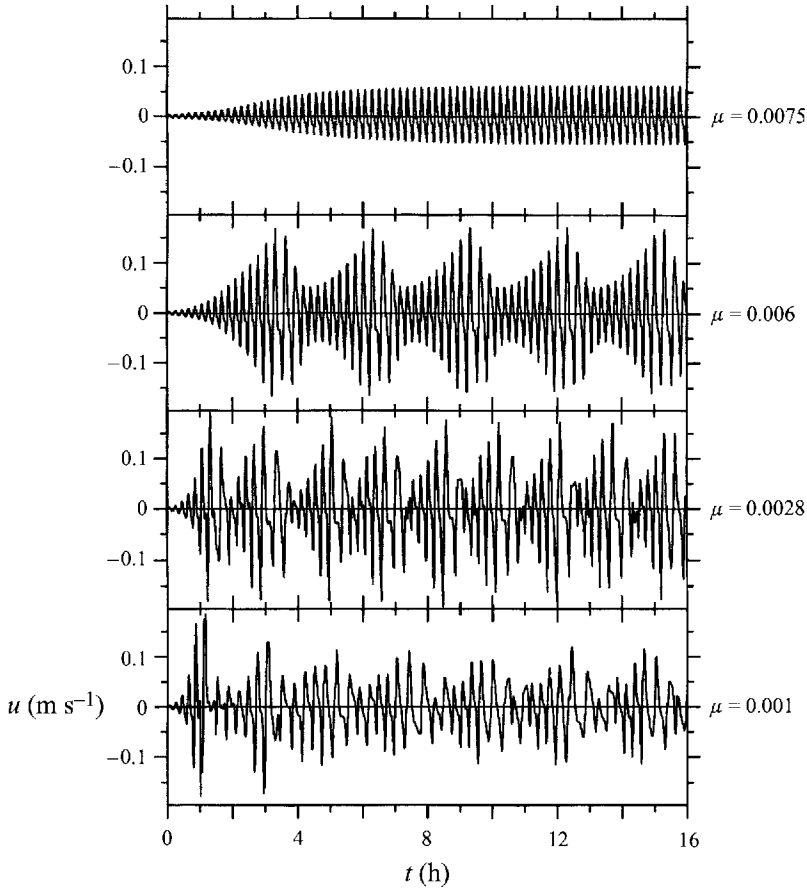
FIGURE 3. Time series of the across-shore velocity component u at $x = 90$ m, $y = \frac{1}{4}L^{(y)} = 112.5$ m from experiments with different values of μ (m s^{-1}) ($n = 3$, $L^{(y)} = 450$ m).

oscillations are associated with nonlinearly equilibrated disturbances of wavelength $2\pi/k = L^{(y)} = 450$ m propagating alongshore in the direction of the forced mean flow. The propagating character of the fluctuations is similar to that shown in figure 8 (described in §5). The propagation velocity is about 0.57 m s^{-1} which is close to the phase speed of the most unstable linear mode. The spatial variability of the disturbances is best illustrated by the vorticity ζ-fields (figure 4) which for $\mu = 0.0075$ show propagating disturbances of essentially constant form. A useful summary of the time variability of the flow is given by contour plots of the alongshore-averaged alongshore velocity $\bar{v}(x, t)$ and the alongshore-averaged perturbation kinetic energy density $\frac{1}{2}(\overline{u'^2 + v'^2})(x, t)$ shown in figure 5. The approximately equilibrated nature of the disturbances for $t > 10$ h is indicated by the non-zero and nearly constant values of $\frac{1}{2}(\overline{u'^2 + v'^2})$.

As μ is decreased further, the character of the fluctuations in u (figure 3) changes. For $\mu = 0.006$, the oscillations in u are of larger magnitude and are modulated in amplitude in a regular manner on a longer time scale of about 3 hours. The high-frequency oscillations correspond to propagating disturbances where the propagation speed is lower for the larger amplitude fluctuations as seen from the slight increase in period. The changes with time of $\bar{v}(x, t)$ and $\frac{1}{2}(\overline{u'^2 + v'^2})$ in figure 5 show that the modulations of $u(t)$ on the longer time scale (figure 3) are related to the
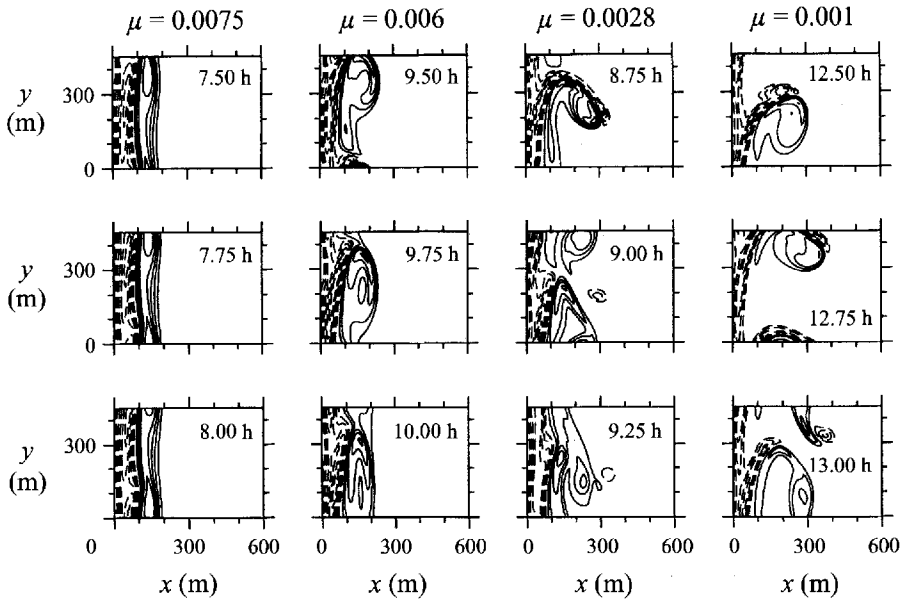
FIGURE 4. Contour plots of the vorticity ζ-fields at times separated by 0.25 h from experiments with different values of μ (m s^{-1}) ($n = 3$, $L^{(y)} = 450$ m). The zero contour is omitted. Solid (dashed) contour lines correspond to negative (positive) values. The contour interval $\Delta\zeta = 0.003$ s^{-1}.

periodic production of perturbation kinetic energy as a result of finite-amplitude instability events. The increases of $\frac{1}{2}(\overline{u'^2 + v'^2})$ with time are accompanied by decreases in magnitude and widening of $\bar{v}(x, t)$. Bottom friction subsequently dissipates the perturbations so that $\frac{1}{2}(\overline{u'^2 + v'^2})$ decreases, the forcing restores $\bar{v}(x, t)$, and the process repeats in a periodic manner. The nature of these instability events is further illustrated by the time-dependent behaviour of the vorticity field (figure 4) which shows disturbances periodically growing and then contracting in the offshore direction.

For $\mu = 0.0028$, the short-period oscillations in u (figure 3) are less regular and the frequency of the modulation is increased compared to the behaviour at $\mu = 0.006$. Again, the fluctuations propagate alongshore, with the larger amplitude fluctuations propagating somewhat slower. The contour plots of $\bar{v}(x, t)$ and $\frac{1}{2}(\overline{u'^2 + v'^2})$ in figure 5 show that the cycle of instability events involving production and subsequent dissipation of perturbation kinetic energy and the corresponding weakening and recovery of $\bar{v}(x, t)$ has increased in frequency. It appears that although the instability events that occur about every 1.75 hours are similar, the process is very close to periodic over two instability events with a period of about 3.5 hours. That aspect of the flow will be discussed further below. The vorticity fields show considerable deformation with time (figure 4) corresponding to a rather complicated shedding of vortices from the unstable jet during the instability events.

As μ is decreased further to $\mu = 0.001$, the oscillations in u (figure 3) become increasingly irregular, but still correspond to alongshore-propagating disturbances with alongshore scale $L^{(y)} = 450$ m and with somewhat similar, but smaller propagation speeds. The overall behaviour still consists of instability events involving the production of bursts of perturbation kinetic energy $\frac{1}{2}(\overline{u'^2 + v'^2})$ accompanied by changes in magnitude of $\bar{v}(x, t)$ (figure 5), but these events appear to occur on an irregular basis with variable intensity. The vorticity fields (figure 4) show wilder and more extensive
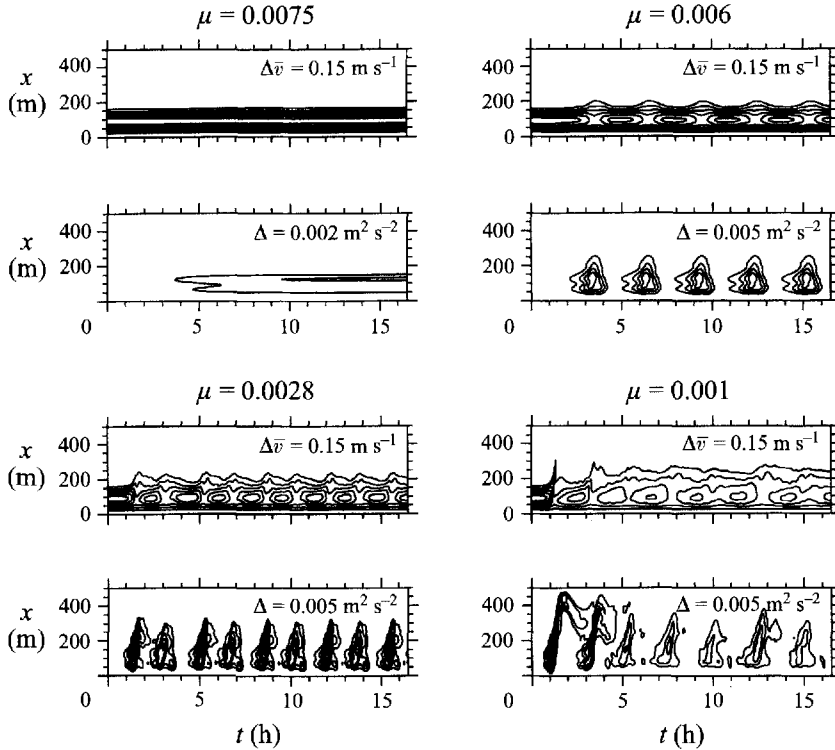
FIGURE 5. Contour plots of alongshore-averaged alongshore velocity $\bar{v}(x,t)$ (upper figures) and the alongshore-averaged perturbation kinetic energy density $\frac{1}{2}(\overline{u'^2} + \overline{v'^2})(x,t)$ (lower figures) as a function of the across-shore coordinate x and time t from experiments with different values of μ (m s^{-1}) ($n = 3$, $L^{(y)} = 450$ m). The contour intervals are $\Delta\bar{v} = 0.15$ m s^{-1}, $\Delta\frac{1}{2}(\overline{u'^2} + \overline{v'^2}) = \Delta = 0.002$ m^2 s^{-2} for $\mu = 0.0075$ and $\Delta = 0.005$ m^2 s^{-2} otherwise.

eddy shedding during the instability events, with previously shed vortices extending farther offshore.

In spite of the changes in flow characteristics as μ is decreased in this set of experiments, the alongshore propagation characteristics given by the linear stability analysis remain a qualitatively robust feature of the response in the fully nonlinear regime.

A further simplification in representing the flow behaviour is provided by examining the time variability of area-averaged quantities. It is of interest to construct a phase-plane representation with the area-averaged perturbation kinetic energy,

$$KE' = \frac{1}{2}\left\{h(\overline{u'^2} + \overline{v'^2})\right\},\tag{4.1}$$

and the area-averaged energy conversion term EC (2.19) as coordinates. Since EC is the physically most important term on the right-hand side of (2.18), this is similar to plotting KE' versus KE'_t. These plots are shown in figure 6 for a large set of experiments with different values of μ. The initial transients are omitted and only the asymptotic large-time behaviour is shown. We see that the behaviour of the forced and frictional fluid dynamical processes in these experiments, as represented in this phase plane, is similar to that found in low-dimensional nonlinear dynamical systems.

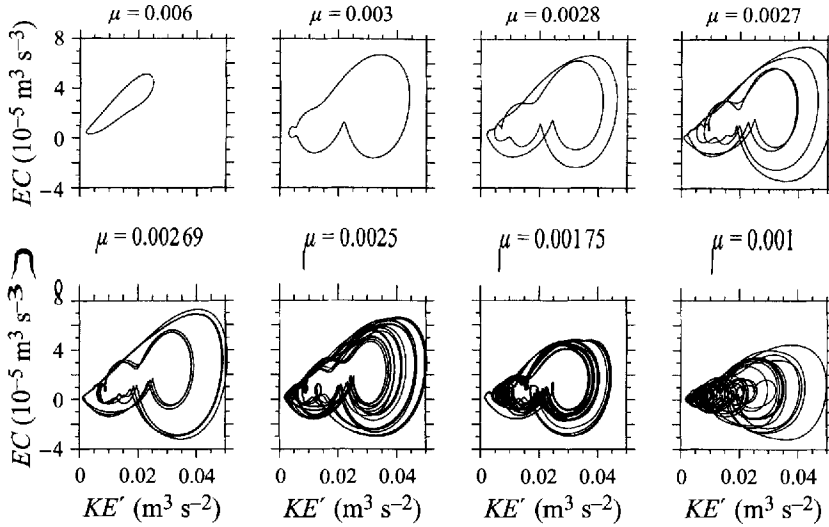For $\mu = 0.01$, the forced alongshore flow is stable. We find $u = 0$ and $KE' = EC = 0$.

FIGURE 6. Phase-plane representation of the large-time behaviour from experiments with different values of μ (m s^{-1}) ($n = 3$, $L^{(y)} = 450$ m). The coordinates are the area-averaged perturbation kinetic energy KE' (4.1) and the area-averaged energy conversion term EC (2.19). Initial transients are omitted to clarify the large-time asymptotic behaviour. Limit cycles have been traced several times.

The large-time state of this system in the (KE', EC) phase plane is a steady solution represented by a point at the origin. For $\mu = 0.0075$, the system is asymptotic to a non-trivial steady solution with non-zero perturbation kinetic energy, corresponding to the steadily propagating disturbances seen in figures 3 and 4, and with non-zero energy conversion. That steady solution is represented in the (KE', EC) phase plane by a point at $(0.0025, 0.7 \times 10^{-5})$. The steady, non-zero energy conversion EC is balanced in (2.18) by frictional dissipation so that $KE'_t = 0$. At $\mu = 0.006$, we find a simple limit cycle reflecting the periodic instability events shown in the $\bar{v}(x,t)$ and $\frac{1}{2}(\overline{u'^2} + \overline{v'^2})$ contour plots in figure 5. A more complicated limit cycle with period about $T = 1.7$ h occurs for $\mu = 0.003$ while at $\mu = 0.0028$ we find that the period of the limit cycle has approximately doubled to 3.5 h, i.e. to about $2T$. That type of periodic behaviour for $\mu = 0.0028$ may be seen in the plots of $\frac{1}{2}(\overline{u'^2} + \overline{v'^2})$ (figure 5) as noted above. For $\mu = 0.0027$, we find that the period of the limit cycle has doubled again to 7.2 h which is approximately $4T$. For $\mu = 0.00269$, we find a clear limit cycle with a period of 10.8 h which is about $6T$. Additional calculations with μ varied between 0.0027 and 0.00269 indicate a bifurcation from period $4T$ to $6T$ near $\mu = 0.002693$. The appearance of a period-$6T$ limit cycle interrupts the period-doubling bifurcation sequence. At lower values of μ, we see irregular behaviour that appears to be associated with a chaotic attractor that changes shape as μ varies through the values 0.0025, 0.00175, 0.001.

We see that, under the conditions of these experiments, this system undergoes the bifurcation sequence $(T \rightarrow 2T \rightarrow 4T \rightarrow 6T)$ before exhibiting irregular oscillations. Consequently, the system does not follow the well known period-doubling cascade as a route to chaos (Feigenbaum 1978, 1983). Interruptions of period-doubling bifurcation sequences by odd-period multiplications have been found in Rayleigh–Bénard experiments with liquid helium by Libchaber & Maurer (1982) and have been discussed by Arneodo et al. (1983). Generally, interrupted cascades can occur in complex systems not necessarily representable by one-dimensional maps. Efforts to quantify the statement that the irregular solutions are chaotic by calculations of the largest

Lyapunov exponent are discussed in Appendix C. It is worth emphasizing the complexity of the potential vorticity dynamics involved in some of the solutions that show regular behaviour in the (KE', EC) phase plane. That is illustrated by the complicated deformations in the vorticity fields during the instability events for $\mu = 0.0028$ (figure 4) that result in a regular period-$2T$ limit cycle in the (KE', EC) plane.

5. Numerical experiments, $n = 3$, $m = 2, 3$

We extend the set of experiments in §4 with $n = 3$ to domains with moderately larger alongshore scales. Two subsets of experiments are run, one with $L^{(y)} = 2(2\pi/k_0) = 900$ m and one with $L^{(y)} = 3(2\pi/k_0) = 1350$ m. In these experiments, the fluid is initially at rest and the forcing V in (2.13) includes small-amplitude perturbations $\epsilon b(y)$ with $\epsilon = 0.01$, $b_j = 1$, and with $J = 2$ (3) for $L^{(y)} = 900$ m (1350 m). This problem corresponds more closely to the time dependence that might occur in the oceanographic situation. We note that when the set of experiments in §4 with $L^{(y)} = 450$ m are conducted in this manner (with $J = 1$), the large-time asymptotic behaviour is qualitatively the same except that the limit cycles are not repeated as precisely because of the weak y-dependence in the forcing. As in §4, we vary the magnitude of the bottom friction μ while all other parameters are held constant. We focus attention on a description of the results from the experiments with $L^{(y)} = 3(2\pi/k_0) = 1350$ m and briefly summarize the results with $L^{(y)} = 2(2\pi/k_0) = 900$ m at the end of the section.

Time series of u at $x = 90$ m, $y = \frac{1}{4}L^{(y)} = 337.5$ m from different experiments with $L^{(y)} = 1350$ m are shown in figure 7. It is clear by comparison of these time series with those in figure 3, that different physical processes occur here for the smaller values of μ. For $\mu = 0.0075$, however, regular alongshore-propagating disturbances with scale $2\pi/k_0$, and with velocity $\simeq 0.57$ m s^{-1}, similar to those found in §4 with $L^{(y)} = 450$ m, grow to near constant amplitude. This is shown in the u time series and in the perspective plot of squared vorticity ζ^2 along $x = 90$ m as a function of y and t in figure 8. The vorticity fields (not shown) reflect propagating disturbances at wavelengths $2\pi/k_0$ that grow and then equilibrate at nearly constant amplitude with structure similar to those found with $\mu = 0.0075$ and $L^{(y)} = 450$ m (figure 4). The contour plots of $\bar{v}(x, t)$ and $\frac{1}{2}(\overline{u'^2} + \overline{v'^2})$ in figure 9 show the rapid development in less than an hour of $\bar{v}(x, t)$ from $\bar{v}(x, t = 0) = 0$ to a profile close to $V_S(x)$. The perturbation kinetic energy density $\frac{1}{2}(\overline{u'^2} + \overline{v'^2})$ builds up more slowly, consistent with the behaviour of u (figure 7), and approaches near steady values after about 15 h. The differences between $\bar{v}(x, t)$ and $V_S(x)$ after about one hour are small, but dynamically significant as demonstrated by the change in linear stability properties of $\bar{v}(x, t)$. Growth rates obtained from linear stability calculations with the basic flow equal to $\bar{v}(x, t)$ at different times are shown in figure 10. As t increases, $\bar{v}(x, t)$ evolves from a profile that is unstable to one that is stable, but very close to marginal stability. The equilibrium of waves of wavelength $2\pi/k_0$ at nearly constant amplitude found here with $\mu = 0.0075$ is in qualitative agreement with the preliminary results reported by Dodd & Thornton (1992) based on weakly nonlinear theory.

For $\mu = 0.007$, regular disturbances of alongshore scale $2\pi/k_0$ grow initially. At about $t = 10$ hours, these disturbances change spatial structure as reflected by the change in character of the fluctuations in u (figure 7). The initial unstable disturbances evolve into a wave group composed of essentially three disturbances with individual wavelengths somewhat smaller than $2\pi/k_0$ and with reduced amplitudes. The wave group nature of the propagation at large time is evident in a perspective plot of
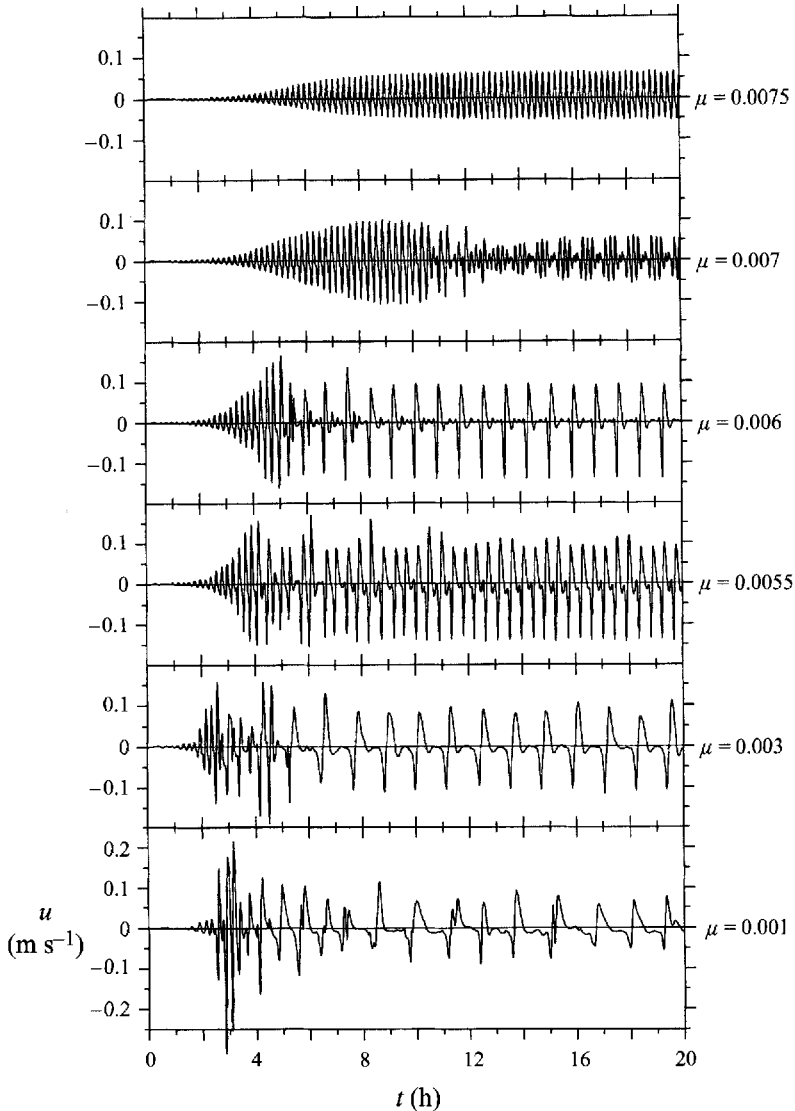
FIGURE 7. Time series of the across-shore velocity component u at $x = 90$ m, $y = \frac{1}{4}L^{(y)} = 337.5$ m from experiments with different values of μ (m s^{-1}) ($n = 3$, $L^{(y)} = 1350$ m).

squared vorticity ζ^2 along $x = 90$ m (not shown). The phase velocity of the individual disturbances ($\simeq 0.55$ m s^{-1}) is greater than the propagation velocity of the group ($\simeq 0.47$ m s^{-1}). As a result, we observe a continuous decrease in amplitude and disappearance of the disturbances at the front of the group and a corresponding appearance and growth in amplitude of the disturbances at the rear of the group.

For $\mu = 0.006$, regular disturbances of alongshore scale $2\pi/k_0$ again grow initially, but after about $t = 5$ h, these break down and form a single longer wavelength disturbance that evolves into a nearly steady propagating nonlinear wave. This process is illustrated in the perspective plot of ζ^2 along $x = 90$ m for $\mu = 0.006$ in figure 8. The breakdown of the initial waves of scale $2\pi/k_0$ and formation of a single disturbance involves selective growth in amplitude and reduction in propagation speed of one of the initial waves. A faster moving, smaller amplitude wave overtakes and merges with
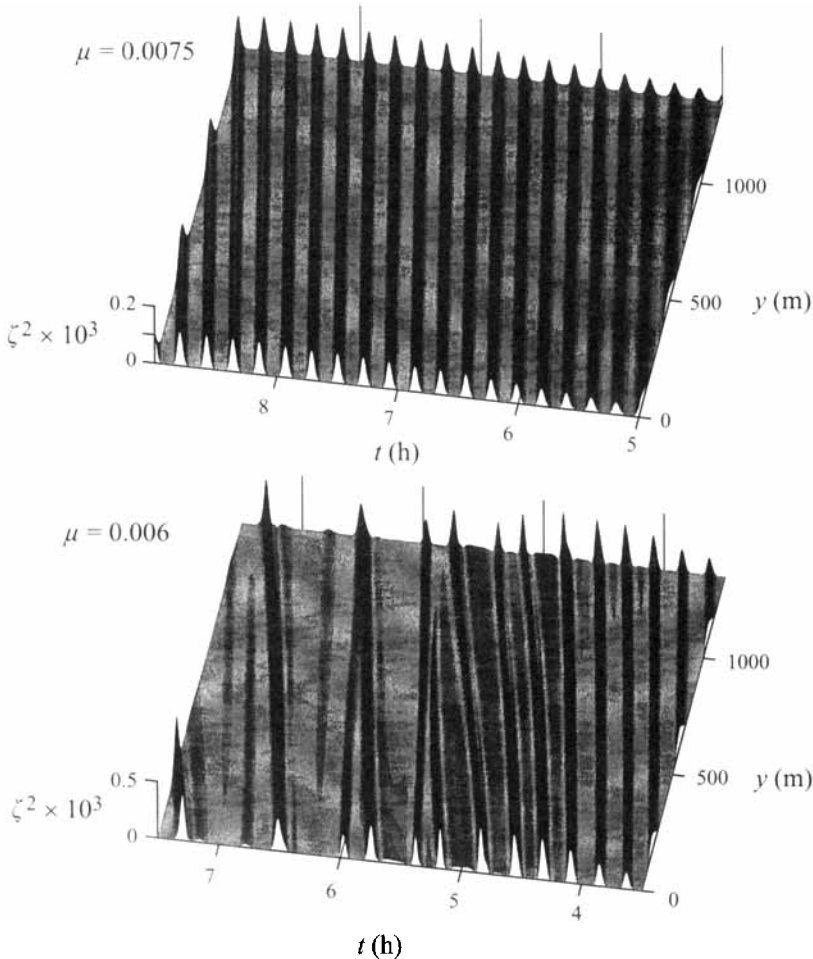
FIGURE 8. Perspective plots of the squared vorticity ζ^2 (s^{-2}) along $x = 90$ m as a function of the alongshore coordinate y and time t for different time periods from the experiments with $\mu = 0.0075$ m s^{-1} and $\mu = 0.006$ m s^{-1} ($n = 3$, $L^{(y)} = 1350$ m).

the larger amplitude wave. The resulting combined disturbance subsequently overtakes and merges with the slower moving, larger amplitude remaining wave. Also illustrated in figure 8, is the reduced propagation speed of the resulting nonlinear disturbance (≈ 0.45 m s^{-1}) compared with that of the initial waves of scale $2\pi/k_0$ (≈ 0.57 m s^{-1}). The changes in the vorticity field during the merger process are shown in figure 11 and illustrate the transition behaviour described above. This process of vortex amalgamation is clearly different than the orbital pairing observed in free shear layers, but may possibly involve a mechanism similar to the 'vortex draining' instability discussed by Klaassen & Peltier (1989). During the transition there is a corresponding change in behaviour of u with time from short-period oscillations of increasing amplitude to longer period oscillations of nearly constant amplitude (figure 7). The near-steady nature of the resulting propagating nonlinear wave may be seen in figure 12. The structure of the vorticity field in the nonlinear wave at $t = 12$ h and $t = 16$ h shows an offshore bulge of negative vorticity with alongshore scale about 400 m at what we will call the front of the wave. This is followed by a long tail of about 950 m length with little alongshore variation in ζ. The behaviour
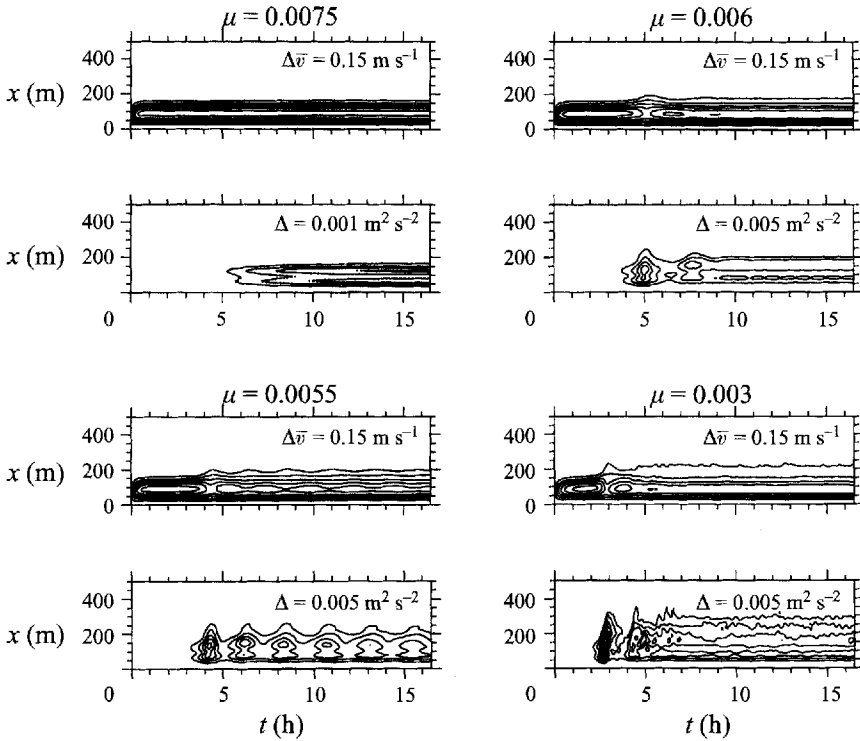
FIGURE 9. Contour plots of $\bar{v}(x,t)$ (upper figures) and $\frac{1}{2}(\overline{u'^2}+\overline{v'^2})(x,t)$ (lower figures) as a function of the across-shore coordinate x and time t from experiments with different values of μ (m s^{-1}) ($n = 3$, $L^{(y)} = 1350$ m). The contour intervals are $\Delta\bar{v} = 0.15$ m s^{-1}, $\Delta\frac{1}{2}(\overline{u'^2}+\overline{v'^2}) = \Delta = 0.001$ m^2 s^{-2} for $\mu = 0.0075$ and $\Delta = 0.005$ m^2 s^{-2} otherwise.

of the flow is also illustrated in the $\bar{v}(x,t)$ and $\frac{1}{2}(\overline{u'^2}+\overline{v'^2})$ contour plots in figure 9 where an instability event, similar to those found for $\mu = 0.006$ with $L^{(y)} = 450$ m and shown in figure 5, occurs starting around $t = 4$ h. Following that event, however, the flow behaviour changes and we see development of a weaker and broader $\bar{v}(x,t)$ accompanied by the establishment of perturbation kinetic energy density $\frac{1}{2}(\overline{u'^2}+\overline{v'^2})$ that has little variation with time, corresponding to the near-steady nature of the propagating nonlinear wave. Profiles of $\bar{v}(x,t)$ at $t = 2$ and $t = 16$ h are plotted in figure 10 and compared with $V_S(x)$. Linear stability results in terms of maximum growth rates versus wavenumber for these profiles are also shown in figure 10. At $t = 2$ h, $\bar{v}(x,t)$ is close to $V_S(x)$ and it has similar linear stability properties. At $t = 16$ h, $\bar{v}(x,t)$ has evolved in the presence of the steady nonlinear wave into a profile that is stable, but very close to marginal stability.

For $\mu = 0.0055$, the initial growing unstable waves are again regular disturbances with alongshore scale $2\pi/k_0$. These break down after about 4 h and evolve into two larger wavelength nonlinear waves as shown by the ζ-fields (figure 12). The breakdown of the initial instabilities of scale $2\pi/k_0$ and evolution into two disturbances involves selective growth of two disturbances, subsequent reduction in propagation speed and merger of one of these with the more rapidly propagating smaller amplitude disturbances. The structure of the vorticity field (figure 12) at the front of the two nonlinear waves, involving an offshore bulge of negative vorticity, is similar to that found at the front of the single wave at $\mu = 0.006$. The two nonlinear waves here are
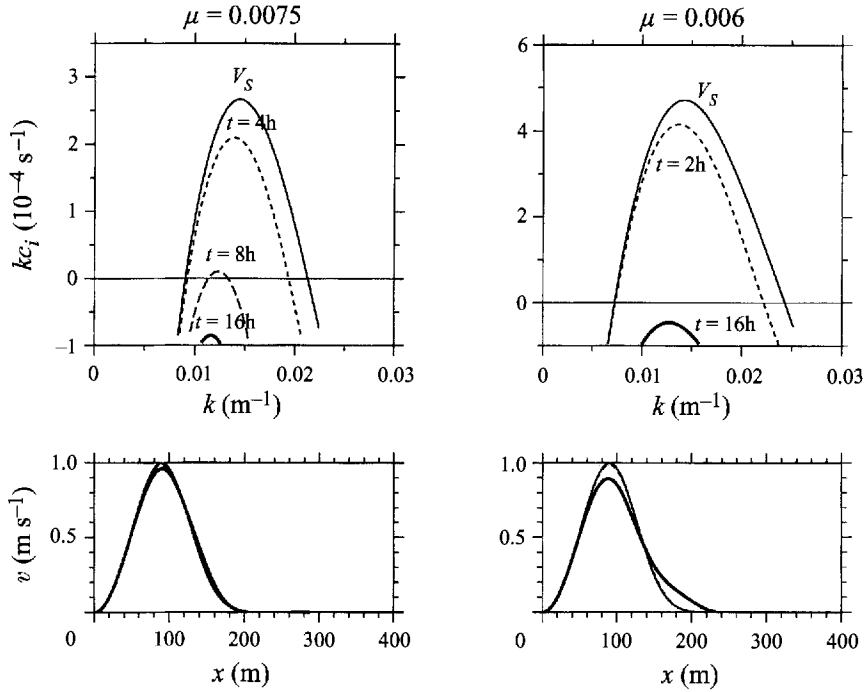
FIGURE 10. Results of linear stability calculations for the basic flow $V_S(x)$ and for $\bar{v}(x,t)$ at different times in terms of growth rate kc_i versus alongshore wavenumber k from the experiments with $\mu = 0.0075$ m s^{-1} and $\mu = 0.006$ m s^{-1} ($n = 3, L^{(y)} = 1350$ m). Also shown are the profiles of $V_S(x)$ and $\bar{v}(x,t)$ at the corresponding times designated by the same line types as kc_i.

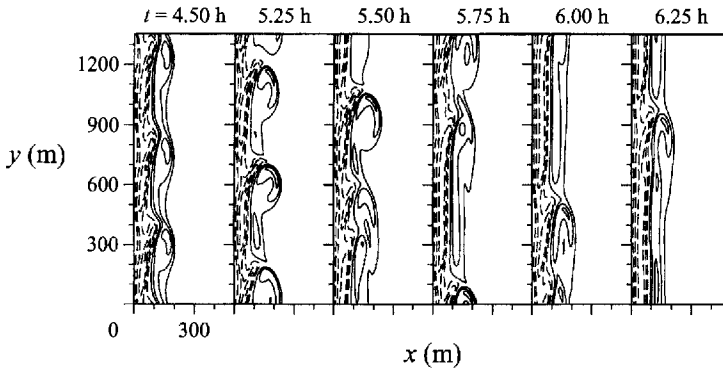FIGURE 11. Contour plots of the vorticity ζ-fields at different times from the experiment with $\mu = 0.006$ m s^{-1} ($n = 3$, $L^{(y)} = 1350$ m). The zero contour is omitted. Solid (dashed) contour lines correspond to negative (positive) values. The contour interval $\Delta\zeta = 0.005$ s^{-1}.

less steady than the single wave at $\mu = 0.006$, however, as shown by a comparison of the time variability in the u time series (figure 7), the $\frac{1}{2}(\overline{u'^2 + v'^2})$ plots (figure 9) and the ζ-fields (figure 12). Fluctuations in $\bar{v}(x,t)$ and $\frac{1}{2}(\overline{u'^2 + v'^2})$ on a longer time scale of about 2.5 h, reminiscent of the behaviour associated with instability events that was found with $L^{(y)} = 2\pi/k_0 = 450$ m, are clearly evident in figure 9. These fluctuations may also be seen as modulations of the amplitude of the higher frequency oscillations in the u time series (figure 7). The emergence at large time of two disturbances at
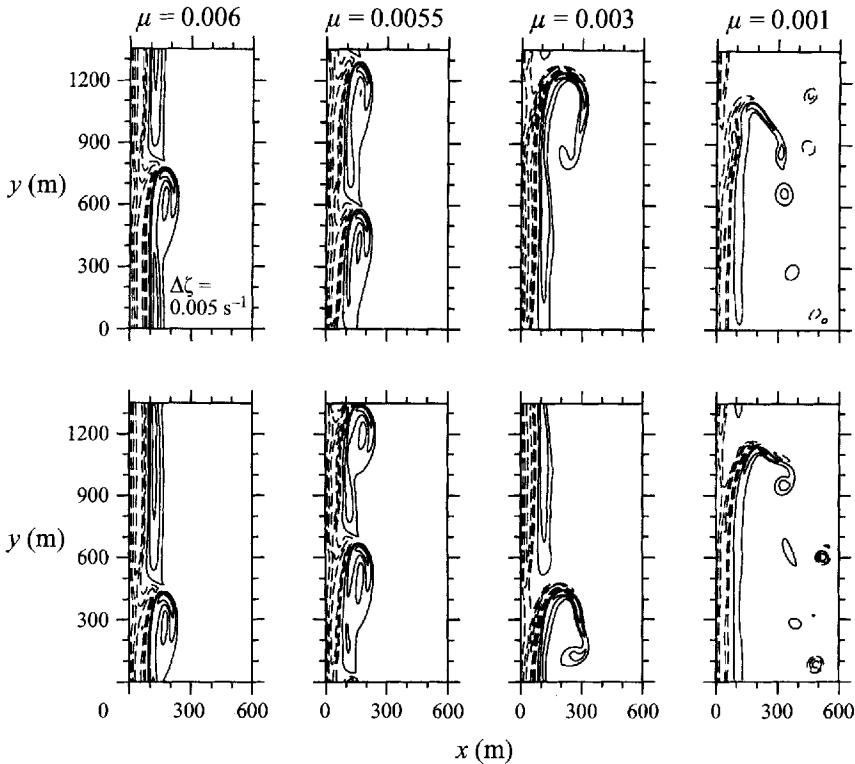
FIGURE 12. Contour plots of the vorticity ζ-fields at times $t = 12$ (top) and 16 h (bottom) from experiments with $\mu = 0.006, 0.0055, 0.003, 0.001$ m s^{-1} ($n = 3, L^{(y)} = 1350$ m). Contours as figure 11.

$\mu = 0.0055$ compared with a single disturbance at larger friction $\mu = 0.006$ and single disturbances at smaller friction values $\mu = 0.003$ and $\mu = 0.001$ (figure 12) seems curious. It turns out, however, that at the friction values $\mu = 0.006$ and $\mu = 0.0055$, the large-time behaviour is not unique and may involve either one or two waves depending on the initial conditions (and presumably also depending on the form of $\epsilon b(y)$ (2.13) which is not varied). This is demonstrated by initializing additional experiments for $\mu = 0.006$ and for $\mu = 0.0055$ with, respectively, the $\mu = 0.0055$, $t = 9$ h fields and the $\mu = 0.006$, $t = 9$ h fields. In both experiments, the single or double wave character of the initial field is preserved in a stable fashion for the ensuing 12 h length of the experiment. The two-wave state at $\mu = 0.006$ has time-dependent variations similar to that found in the two-wave state at $\mu = 0.0055$ while the single wave state at $\mu = 0.0055$ shows near-steady behaviour similar to that found in the single wave at $\mu = 0.006$.

At the lower value of $\mu = 0.003$, the breakdown of growing initial disturbances with wavelength $2\pi/k_0$ occurs relatively quickly as shown by the behaviour of the u time series in figure 7. A long-wavelength nonlinear disturbance develops by about 5.5 h. The propagation speed of this disturbance is about 0.27 m s^{-1} and is slower than that of the nonlinear wave at $\mu = 0.006$ as evidenced by the increased period of the u oscillations (figure 7). The propagating nonlinear wave at $\mu = 0.003$ has an unsteady character that is shown by the time variation of the vorticity fields in figure 12. Also evident in the vorticity fields is the increased distance offshore to which the negative vorticity fluctuations extend compared with the $\mu = 0.006$ case. The irregularity in time of the propagating disturbance with $\mu = 0.003$ is also indicted by the time

variations of the perturbation kinetic energy density $\frac{1}{2}(\overline{u'^2} + \overline{v'^2})$ in figure 9. The effects of the time-dependent nonlinear disturbance in broadening and weakening the alongshore-average velocity field $\bar{v}(x, t)$ compared to $V_S(x)$ are also evident in figure 9.

For $\mu = 0.001$, the behaviour is qualitatively similar to that found at $\mu = 0.003$ except that the propagating nonlinear disturbances are more irregular in time and space and generally propagate slower. The vorticity fields (figure 12) show the result of increased shedding of vortices and the presence of these previously shed vortices at offshore locations up to 500 m from the coast.

It is instructive to examine and compare aspects of the potential vorticity balance in the steady, equilibrated waves of wavelength $2\pi/k_0$ found for $\mu = 0.0075$ and in the longer wavelength, nearly steady, nonlinear wave found with $\mu = 0.006$. For this purpose we utilize the decomposition of the potential vorticity (2.20a) $q = \bar{q} + q'$ and consider the equation (2.22) for q' transformed to a coordinate system moving at the observed speed of the wave c. Accordingly, in terms of the coordinates

$$s = t, \quad \eta = y - ct, \tag{5.1a, b}$$

(2.22) transforms to

$$q'_s + u'\bar{q}_x + (\bar{v} - c)q'_\eta + u'q'_x + v'q'_\eta - (\overline{u'q'_x} + \overline{v'q'_\eta})$$

$$+ (\mu/h)[(v'/h)_x - (V'/h)_x - (u'/h)_\eta] + (v/h)\nabla^4\zeta' = 0, \tag{5.2}$$

where η replaces y in the ∇^4 operator.

We consider an alongshore position y_0 for each wave at large time t_0 and examine the balance of terms in (5.2) as a function of x in figure 13. Also shown in figure 13 are the values of $\bar{\zeta}, \zeta', v'_x$, and $-u'_y$ at y_0 and t_0 and the balance of terms in equation (2.21) for $\bar{q}$ at t_0. Calculation of these terms is described in Appendix B. The alongshore position y_0 is chosen to be a location where the vorticity field in the wave has interesting structure. For $\mu = 0.0075$ we choose $y_0 = 100$ m at $t_0 = 30$ h. This position in the wave corresponds approximately to $y = 50$ m in the similar vorticity field at $t = 8$ h for $\mu = 0.0075$ with $L^{(y)} = 450$ m (figure 4). For $\mu = 0.006$, we choose $y_0 = 50$ m at $t_0 = 20$ h which corresponds to about $y = 350$ m at 16 h (figure 12). This location is near the front of the offshore bulge in vorticity at the front of the wave.

For $\mu = 0.0075$, the perturbation vorticity ζ' is generally smaller in magnitude than $\bar{\zeta}$. In addition, $-u'_y$ is generally small in magnitude compared to v'_x. Consequently, ζ' is almost entirely represented by v'_x, which is a characteristic of a long wave. For $\mu = 0.006$, ζ' is comparable in magnitude to $\bar{\zeta}$. Also, $-u'_y$ is comparable in magnitude to v'_x and makes a substantial contribution to ζ' between about 150 m and 200 m offshore, which is consistent with the impression from the structure of the vorticity field. In (5.2) we characterize the degree of nonlinearity present in the wave by the relative magnitude of the terms $u'q'_x + v'q'_\eta - (\overline{u'q'_x} + \overline{v'q'_\eta})$ which represent the advection of perturbation potential vorticity q' by the perturbation velocity components u' and v'. For $\mu = 0.0075$, these terms are non-negligible but generally smaller than the other terms, possibly corresponding to a weakly nonlinear equilibration. In contrast, for $\mu = 0.006$ these terms play a dominant role in the balance between about 50 m to 230 m offshore indicating the presence of relatively strong nonlinear effects. Note also that with $\mu = 0.006$ the bottom friction terms are smaller relative to the other terms than with $\mu = 0.0075$. The terms in equation (2.21) for $\bar{q}$ show $\bar{q}_t \simeq 0$ for both $\mu = 0.0075$ and $\mu = 0.006$. Within 20 m of the coast, the biharmonic friction term $(v/h)\nabla^4\bar{q}$ balances $(\mu/h)[(\bar{v} - V_S)/h]_x$. Offshore of about $x = 20$ m, the biharmonic
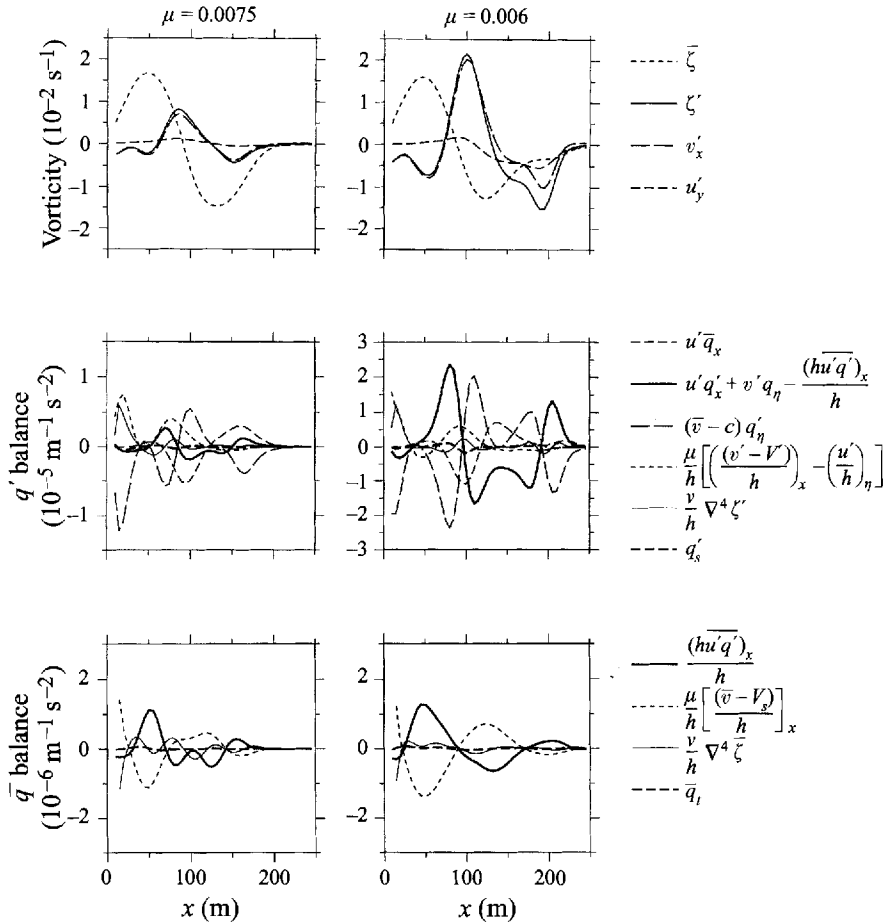
FIGURE 13. The alongshore-averaged vorticity $\bar{\zeta}$, the perturbation vorticity ζ', v'_x, and $-u'_y$ as a function of x at alongshore position y_0 and time t_0 from the experiments with $\mu = 0.0075$ m s^{-1} and $\mu = 0.006$ m s^{-1} ($n = 3$, $L^{(y)} = 1350$ m). Also shown as a function of x are the terms in the potential vorticity equation for q' (5.2) at the same y_0 and t_0 and the terms in the potential vorticity equation for $\bar{q}$ (2.21). For $\mu = 0.0075$, $y_0 = 100$ m, $t_0 = 30$ h and $c = 0.57$ m s^{-1}. For $\mu = 0.006$, $y_0 = 50$ m, $t_0 = 20$ h and $c = 0.45$ m s^{-1}.

friction term is relatively small and the dominant balance is given by (2.24) where the difference between $\bar{v}$ and V_S, which corresponds to a broadening and weakening of $\bar{v}$ relative to V_S (figure 10), is forced by the alongshore-averaged across-shore flux of perturbation potential vorticity.

We turn our attention next to the subset of experiments with $L^{(y)} = 2(2\pi/k_0) = 900$ m. In light of the importance of vortex pairing observed in two-dimensional unstable free shear layers and the proposed relation of that behaviour to secondary instabilities involving the first subharmonic of Kelvin–Helmholtz instability waves (e.g. Ho & Huerre 1984; Klaassen & Peltier 1989), it seems logical to conduct experiments here with $L^{(y)} = 2(2\pi/k_0)$ varying μ over the same values as in the $L^{(y)} = 3(2\pi/k_0)$ experiments. Qualitatively similar behaviour is found.

For $\mu = 0.0075$, waves of wavelength $2\pi/k_0$ grow and equilibrate with nearly steady amplitudes as found with $L^{(y)} = 1350$ m. The response for $\mu = 0.007$ consists of waves that grow at wavelength $2\pi/k_0$ and, for the most part, remain at that wavelength

with amplitudes that vary slowly in time. This contrasts with the development of smaller amplitude wave group disturbances found at large time with $L^{(y)} = 1350$ m. For $\mu \leqslant 0.006$, waves of wavelength $2\pi/k_0$ grow initially. The amplitudes equilibrate with low-frequency modulations and exhibit behaviour similar to that found with $L^{(y)} = 450$ m. After two or three of the longer period cycles, however, these waves break down and evolve into nearly steady or unsteady propagating disturbances with alongshore length scale $L^{(y)} = 900$ m.

For $\mu \leqslant 0.006$, the vorticity fields at large time from the experiments with $L^{(y)} = 900$ m are similar to those found with $L^{(y)} = 1350$ m. The structure at the front of the disturbances, where the negative vorticity extends offshore, has length scales in both the alongshore and across-shore directions that are close to the scales at the front of the corresponding disturbances found with $L^{(y)} = 1350$ m (figure 12). The time variations associated with the offshore vorticity fluctuations at the front of the wave for the lower values of μ are likewise similar. The major differences occur in the greater lengths of the tail regions of the waves found with $L^{(y)} = 1350$ m.

We note that the transition for $\mu \leqslant 0.006$ from waves of wavelength $2\pi/k_0$ into nonlinear disturbances with larger alongshore scale occurs quite a bit more rapidly with $L^{(y)} = 1350$ m than with $L^{(y)} = 900$ m. Since the perturbations in $\epsilon b(y)$ (2.13) have the same magnitude in the two sets of experiments with different $L^{(y)}$, this suggests that secondary instabilities of the initial disturbances that involve the first subharmonic of wavelength $2(2\pi/k_0)$ (which is not present in the experiments with $L^{(y)} = 1350$ m) do not play a pivotal role in the transition process.

The fact that for $\mu \leqslant 0.006$ the alongshore scales of the large-time, nonlinear disturbances in most of the experiments are found to be equal to the domain scale $L^{(y)}$ leaves unanswered an obvious question concerning the natural scales of these disturbances when they are not restricted by the size of the domain. That question is addressed in the next section.

6. Numerical experiments, $n = 6$, $m = 10, 12$

In this set of experiments, we utilize domains with alongshore scales that are substantially larger than the wavelength of the most unstable linear mode, i.e. $m = 10$ or $m = 12$ in (2.14). The primary objective here is to obtain information about the preferred alongshore scale of the disturbances at the values of μ for which they evolve into long-wavelength nonlinear waves. The $V_S(x)$ profile in the forcing (2.13) is that with $n = 6$ so that $2\pi/k_0 = 180$ m (figure 2). Two subsets of experiments are run, one subset with $L^{(y)} = 10(2\pi/k_0) = 1800$ m and another with $L^{(y)} = 12(2\pi/k_0) = 2160$ m. As in §5, in these experiments the fluid is initially at rest and the forcing V in (2.13) includes small-amplitude perturbations $\epsilon b(y)$ with $\epsilon = 0.001$, $b_j = 1$, and with $J = 10$ (12) for $L^{(y)} = 1800$ m (2160 m). The magnitude of μ is varied while the other parameters are held constant at the same values as before. For a given value of μ we first discuss the results from the experiments with $L^{(y)} = 1800$ m and follow with a comparison to the corresponding results with $L^{(y)} = 2160$ m.

Time series of u at $x = 90$ m, $y = \frac{1}{4}L^{(y)} = 450$ m from the experiments with $L^{(y)} = 1800$ m are shown in figure 14. Corresponding time series of u at $x = 90$ m, $y = \frac{1}{4}L^{(y)} = 540$ m from the experiments with $L^{(y)} = 2160$ m are also shown in figure 14. For $\mu = 0.017$ and $L^{(y)} = 1800$ m, nine disturbances of wavelength about 200 m grow slowly and eventually equilibrate. These result in high-frequency oscillations in u with a period of about 7 min (figure 14). The modulation in the amplitude of
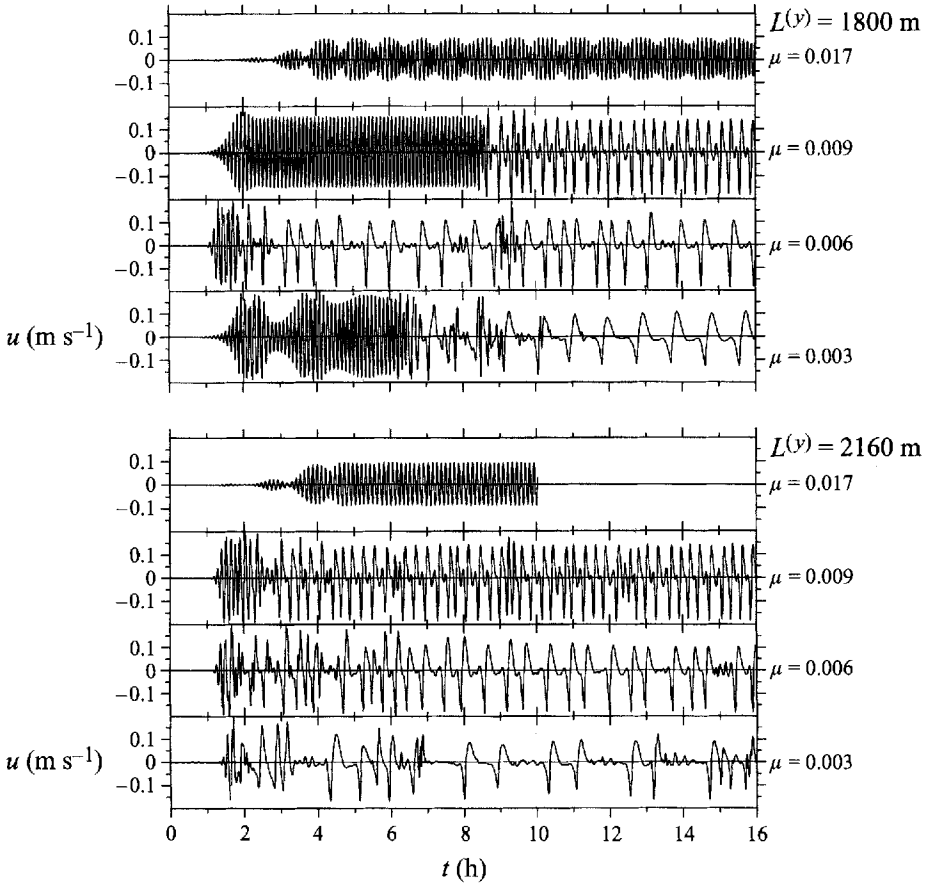
FIGURE 14. Time series of the across-shore velocity component u at $x = 90$ m, $y = \frac{1}{4}L^{(y)} = 450$ m ($n = 6$, $L^{(y)} = 1800$ m) and at $x = 90$ m, $y = \frac{1}{4}L^{(y)} = 540$ m ($n = 6$, $L^{(y)} = 2160$ m) from experiments with different values of μ (m s^{-1}).

u on the longer time scale of about an hour is caused by a continuous large-scale spatial variation of the strength of the nine waves. The growth of instabilities at wavelengths about 200 m is consistent with the decrease of the wavenumber of the most unstable linear mode as μ increases (figure 2). In an experiment with $\mu = 0.017$ and $L^{(y)} = 2160$ m, we find that ten waves of wavelength 216 m grow and equilibrate at a similar amplitude, but without the longer period modulation. Thus, the large-scale spatial amplitude modulation found with $L^{(y)} = 1800$ m is presumably directly related to the alongshore scale of the domain even though $L^{(y)}$ is relatively large compared to $2\pi/k_0$.

For $\mu = 0.009$ and $L^{(y)} = 1800$ m, ten waves of wavelength 180 m grow and equilibrate after about 2.5 h. Around $t = 8.5$ h these waves evolve into four nonlinear waves with alongshore scales between about 350 m and 500 m. At large time, the amplitudes and alongshore scales vary among the four nonlinear waves as shown by the vorticity field at $t = 12$ h (figure 15), but they remain reasonably steady in time as indicated by the near repeatability of the u time series after $t = 11$ h (figure 14). The vorticity fields in the four dominant waves are qualitatively similar to those found previously with $n = 3$ and $L^{(y)} = 1350$ m in §5 (figure 12) but with smaller alongshore scales. There is an offshore bulge of negative vorticity over an alongshore scale of
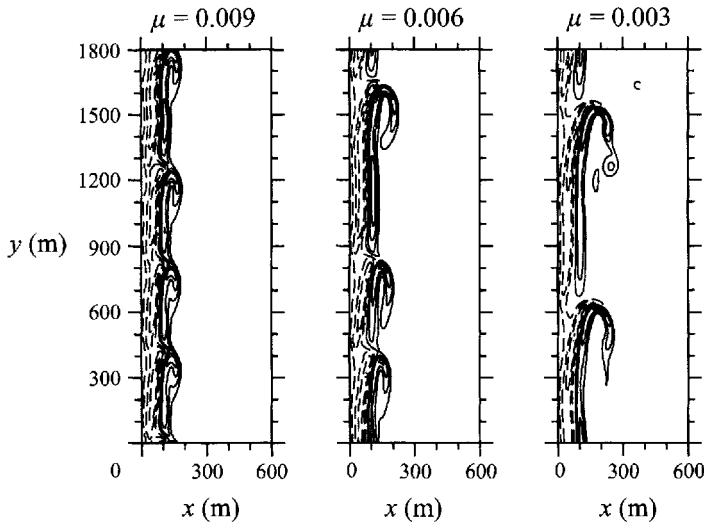
FIGURE 15. Contour plots of the vorticity ζ-fields at time $t = 12$ h from experiments with $\mu = 0.009$, 0.006, 0.003 m s^{-1} ($n = 6$, $L^{(y)} = 1800$ m). The zero contour is omitted. Solid (dashed) contour lines correspond to negative (positive) values. The contour interval $\Delta\zeta = 0.005$ s^{-1}.

roughly 200 m at the front of the wave, followed by a more uniform tail region with an alongshore scale also around 200 m. In an experiment with $\mu = 0.009$ and $L^{(y)} = 2160$ m, we find qualitatively similar large-time behaviour with the formation of five nonlinear waves with alongshore scales of about 430 m. In that case, the breakdown of the initial waves of length 180 m and the formation of the nonlinear waves occurs much earlier, around $t = 3$ h.

For $\mu = 0.006$ and $L^{(y)} = 1800$ m, waves of length 180 m grow initially, but very rapidly break down into long-wavelength propagating nonlinear waves. The nonlinear disturbances form, merge and interact in a complicated manner such that at different times two, three, or four separate individual disturbances with alongshore scales ranging from about 200 m to 900 m are observed. At $t = 12$ h, for example, three disturbances are present in the vorticity field (figure 15). The changes in the vorticity field with time are reflected by the variations in the periods of the oscillations in the u time series (figure 14). The nature of the time-dependent change in structure of the waves is shown in the perspective plots of $\zeta^2(y, t)$ in figure 16. Two time periods are shown. During the first time period (10.5 to 14.5 h), three disturbances evolve into two. This occurs through a reduction in amplitude and increase in propagation velocity of one of the disturbances followed by a merger at about $t = 12.75$ h of that disturbance with one of the original slower moving ones. During the second time period (16–20 h), the two disturbances that resulted at the end of the first period evolve into three. It may be seen that small-amplitude faster propagating disturbances form and grow in one of the regions between the two initial disturbances. These eventually develop into two new finite-amplitude disturbances, one of which merges at about $t = 19$ h with one of the original waves and one of which grows into a separate third disturbance. Consequently, in this experiment the number and the alongshore scales of the nonlinear disturbances vary in an irregular manner. Similar results are found in the corresponding experiment at $\mu = 0.006$ with $L^{(y)} = 2160$ m.

For $\mu = 0.003$ and $L^{(y)} = 1800$ m, we find initial growth and equilibration of waves of wavelength 180 m. After about $t = 6$ h, these waves break down and
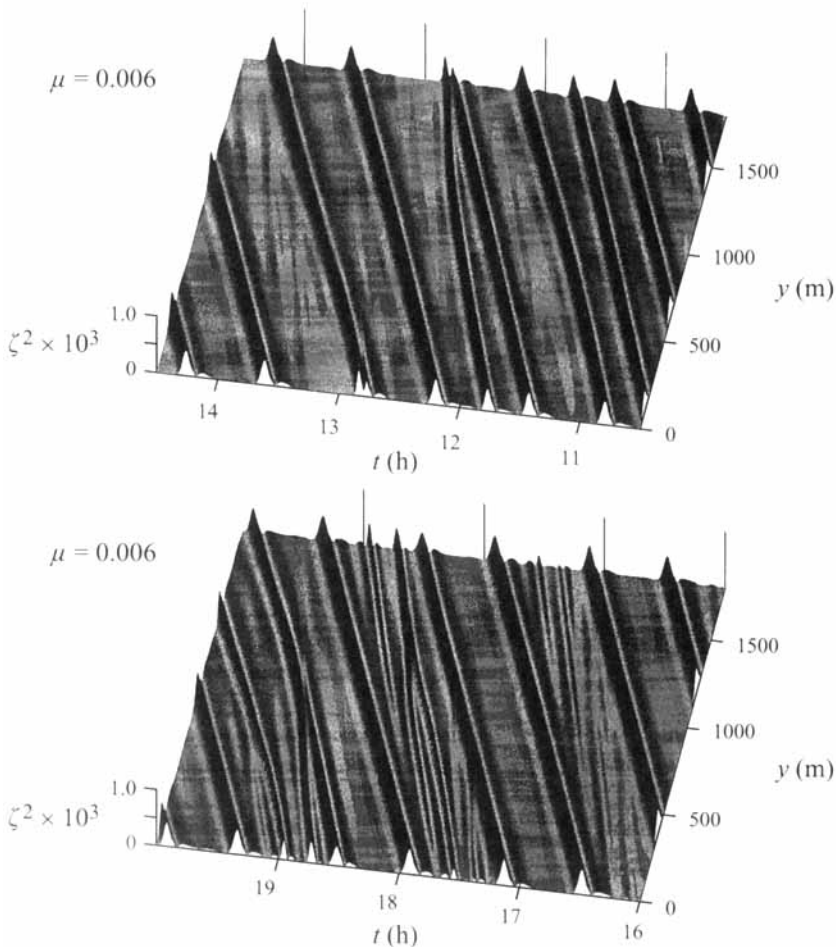
FIGURE 16. Perspective plots of the squared vorticity ζ^2 (s^{-2}) along $x=90$ m as a function of alongshore coordinate y and time t for two time periods from the experiment with $\mu = 0.006$ m s^{-1} ($n = 6$, $L^{(y)} = 1800$ m).

eventually by $t = 9$ h form two unsteady propagating nonlinear disturbances with alongshore scales that fluctuate around 900 m (figure 15) and with propagation velocities that fluctuate around 0.27 m s^{-1}. Generally similar behaviour is found in an experiment with $\mu = 0.003$ and $L^{(y)} = 2160$ m, except that the breakdown into larger-scale disturbances occurs almost immediately after 2 h. With $L^{(y)} = 2160$ m, two disturbances are found most of the time, e.g. around $t = 4$ h and from $t = 7$ h to $t = 14$ h. The alongshore scales of these disturbances and the offshore extension of negative vorticity at the front of the waves fluctuate more strongly and more irregularly in time than with $L^{(y)} = 1800$ m. The alongshore scales vary between about 700 m and 1400 m. In addition, occasionally, e.g. around $t = 6$ h and $t = 15$ h, additional disturbances form and grow so that the total number is three or four. These evolve, however, back into two large-scale disturbances on a 1–2 h time scale.

In general, comparisons of the results of the experiments with $L^{(y)} = 1800$ m with those for $L^{(y)} = 2160$ show similarity of the major qualitative features of the behaviour. The differences found in the specifics of the response indicate that some dependence on the alongshore scale of the domain remains. Part of that dependence,
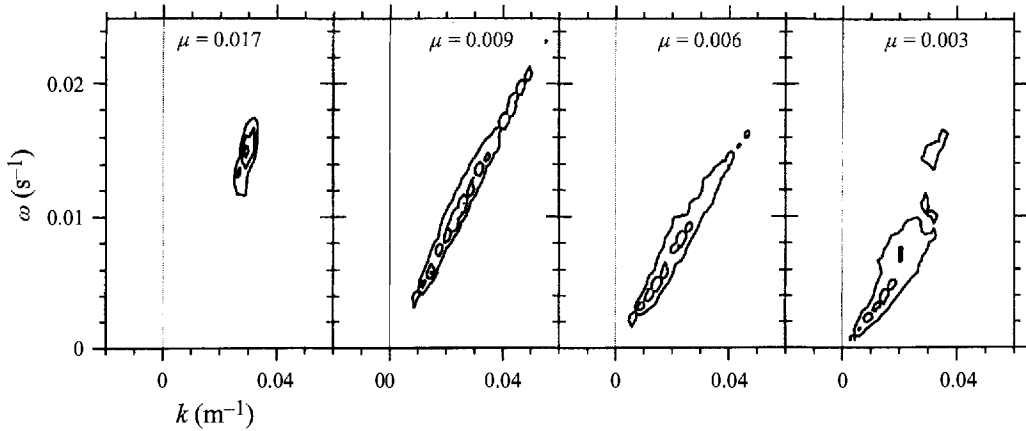
FIGURE 17. Wavenumber–frequency (k, ω) spectra for the across-shore velocity component $u(y, t)$ at $x = 90$ m from experiments with different values of μ (m s^{-1}) ($n = 6$, $L^{(y)} = 2160$ m). Spectra are calculated for the 5 h time period (5–10 h) for $\mu = 0.017$ m s^{-1} and for the 10 h time period (6–16 h) for $\mu = 0.009$, 0.006 and 0.003 m s^{-1}. The spectra are smoothed by averaging over 5 frequencies. The contours plotted are 1×10^{-4}, 1×10^{-5}, and 1×10^{-6} m^2 s^{-2}.

however, is likely due to the unstable nature and corresponding sensitive dependence on exact conditions of the evolving flow fields. The results concerning preferred alongshore scales of the nonlinear disturbances are similar from both subsets of experiments. These scales were found to increase from a range around 350–500 m for $\mu = 0.009$ to a range around 700–1400 m for $\mu = 0.003$, with a regime found for $\mu = 0.006$ where the scales varied in a time-dependent manner between about 200 m and 900 m. In general, the smaller the friction the longer the alongshore scale.

To obtain a better appreciation of how these nonlinear disturbances might appear in data from field experiments, we plot in figure 17 alongshore wavenumber–frequency (k, ω) spectra calculated for the across-shore velocity component $u(y, t)$ at $x = 90$ m from the experiments with $L^{(y)} = 2160$ m. For $\mu = 0.017$, the energy is concentrated around $k_M = 0.029$ m^{-1} and $\omega_M = 0.015$ s^{-1}, with corresponding wavelength $2\pi/k_M = 216$ m, period $2\pi/\omega_M = 0.12$ h, and phase velocity $c_M = \omega_M/k_M = 0.52$ m s^{-1}. For lower values of μ, the energy is distributed over a wider range of ω and k, but is rather tightly confined to a narrow region around a line given approximately by $\omega = c_M k$. As μ decreases, c_M decreases and the energy distribution moves to lower values of ω and k. For $\mu = 0.009, 0.006$, and 0.003, we find $c_M = 0.40$, 0.34 and 0.26 m s^{-1}, respectively. Consequently, the wavenumber–frequency spectra show propagation of all these disturbances in a nearly non-dispersive manner, with differentiation of the behaviour indicated primarily by the inferred propagation velocities and relative distribution of energy with ω and k.

7. Summary

The behaviour of the flow over plane beaches in the idealized, forced, dissipative problems considered here depends on the value of the dimensionless parameter Q (2.4), which represents the ratio of an advective to a frictional time scale. The dependence on a single parameter Q (in the limit $R^{-1} \ll 1$) provides considerable economy in characterizing the nature of the response. For a given across-shore structure in the forcing and given dimensionless alongshore scale of the domain, the range of

behaviour of the flow is given by a complete set of solutions for different values of Q. Solutions for specific dimensional cases with different values for the beach slope h_0/L, the friction coefficient μ, or the magnitude of the forcing V_{SM}, may be extracted at the appropriate value of Q from that solution set (Appendix A). Consequently, it is appropriate to discuss the results in terms of variations in Q.

The steady frictionally balanced alongshore current that would be set up by the assumed forcing in the absence of instabilities is linearly unstable for Q less than a critical value Q_C. Three sets of numerical experiments are conducted to determine the dependence of the flow on $\Delta Q = Q_C - Q$ and on the alongshore scale of the domain $L^{(y)}$ expressed in units of wavelengths of the most unstable linear mode $2\pi/k_0$. A rich variety of different phenomena is found.

In the first set of experiments, the forcing $V_S(x)$ (2.13b) has $n = 3$ and $L^{(y)} = (2\pi/k_0) = 450$ m. We find that for small, positive $\Delta Q = Q_C - Q$, alongshore-propagating disturbances grow and equilibrate at nearly constant amplitude with propagation velocity close to that given by linear stability analysis. For larger ΔQ, periodic finite-amplitude instability events occur resulting in regular modulations of the amplitudes of the propagating disturbances on a longer, several hour time scale. As ΔQ is increased, periodic behaviour is found involving two instability events at first, then four, and then six. When ΔQ is increased further, we find that the events and their amplitudes vary irregularly in time. Representation of the flow evolution in a phase plane with area-averaged perturbation kinetic energy KE' and the area-averaged energy conversion term EC as coordinates shows that the behaviour of the forced dissipative fluid dynamical processes in these experiments has similarities to the behaviour found in low-dimensional nonlinear dynamical systems, including the existence of non-trivial steady solutions, bifurcation to a limit cycle, two period-doubling bifurcations, and irregular chaotic oscillations. We find that the period-doubling cascade is interrupted to give a bifurcation sequence $(T \to 2T \to 4T \to 6T)$ before the irregular oscillations occur. Although the characteristics of the flow change as ΔQ is increased, the alongshore propagation of fluctuations with scale $2\pi/k_0$ remains a strong qualitative feature of the response.

In the second set of experiments, the alongshore scale at the domain is extended so that $L^{(y)} = 2$ $(2\pi/k_0)$ or $L^{(y)} = 3(2\pi/k_0)$. The forcing is (2.13) with $n = 3$, for which $Q_C = 0.19$. The fluid is initially at rest. We find that for positive ΔQ, alongshore-propagating disturbances play a major role in the response of the fluid. For most values of ΔQ, however, these disturbances have a different character than we find when the alongshore scale of the domain is restricted to $2\pi/k_0$. In the subset of experiments with $L^{(y)} = 3(2\pi/k_0)$, we find that for ΔQ small and positive, fluctuations of wavelength $2\pi/k_0$ grow and equilibrate at nearly constant amplitude. The alongshore-averaged alongshore velocity $\bar{v}(x,t)$ in the equilibrated state is steady and near marginal stability for linear perturbations. It is perhaps worth pointing out that if a similar phenomenon occurred in the ocean, an accurate time-averaged alongshore current profile obtained from measurements would not be judged unstable by a linear stability analysis. For larger positive ΔQ, waves of wavelengths $2\pi/k_0$ grow initially, but subsequently evolve into nonlinear, finite-amplitude, nearly steadily propagating disturbances with alongshore scale equal to the domain length $3(2\pi/k_0)$. These disturbances are characterized by a bulge of negative vorticity, extending offshore about 200 m with an alongshore scale of about 400 m, at the front of the wave. This is followed by a longer tail region of about 900 m with little alongshore variation in vorticity. The alongshore-averaged alongshore velocity $\bar{v}(x,t)$ evolves to a nearly steady profile that again is near marginal stability for linear perturbations.

For increased values of ΔQ, the disturbances become unsteady with the negative vorticity at the front of the wave extending farther offshore and fluctuating in time. A range of ΔQ values is found in which the large-time behaviour depends on the initial conditions and may involve a single, nearly steady nonlinear wave with alongshore scale $3\,(2\pi/k_0)$ or may involve two less steady waves with alongshore scales around $(3/2)(2\pi/k_0)$. In general, the larger the amplitude of the disturbance, the slower the propagation speed. In the subset of experiments with $L^{(y)} = 2(2\pi/k_0)$, similar qualitative behaviour occurs concerning the transition waves of wavelength $2\pi/k_0$ into single, nonlinear, propagating disturbances with alongshore scale $L^{(y)}$. The transitions appear to develop less readily in these experiments, i.e. they occur at larger time, suggesting that secondary instabilities involving the first subharmonic of wavelength $2(2\pi/k_0)$ are not critical components of the transition.

In the third set of experiments, the alongshore scale of the domain is substantially larger than the wavelength of the most unstable linear mode with $L^{(y)} = 10(2\pi/k_0)$ or $L^{(y)} = 12(2\pi/k_0)$. The objective is to find the preferred alongshore scale of the disturbances that evolve into finite-amplitude nonlinear waves. In these experiments, we utilize $V_S(x)$ with $n = 6$ in the forcing (2.13) so that $2\pi/k_0 = 180$ m and $Q_C = 0.5$. The fluid is initially at rest. The dependence of the flow behaviour on ΔQ is qualitatively similar to that found in the second set of experiments. For small positive ΔQ, disturbances with alongshore scales close to $2\pi/k_0$ grow and equilibrate at large time. The equilibrated state may involve a regular spatial modulation or irregular fluctuations in space and time of the amplitudes of the disturbances. The range of ΔQ for which the disturbances retain alongshore scales close to $2\pi/k_0$ at large time is somewhat greater than in the second set of experiments, but Q_C is greater here also. The general tendency at moderate values of ΔQ for fluctuations that grow initially at wavelength $2\pi/k_0$ to evolve into more slowly propagating finite-amplitude disturbances with alongshore scales greater than $2\pi/k_0$ is found in this set of experiments also. The alongshore scales of the nonlinear disturbances increase as ΔQ increases from around 350–500 m at $\Delta Q = 0.28$ ($\mu = 0.009$) to 700–1400 m at $\Delta Q = 0.44$ ($\mu = 0.003$). One regime is found at $\Delta Q = 0.38$ ($\mu = 0.006$), where the nonlinear disturbances continuously form, merge and interact in a complicated time-dependent manner such that their alongshore scales vary irregularly in time between about 200 m and 900 m.

In summary, for small positive ΔQ, we find that the flow at large time typically contains equilibrated, steady or unsteady, finite-amplitude disturbances propagating alongshore in the direction of the forced current with wavelengths and propagation velocities close to those indicated by a linear stability analysis of $V_S(x)$. For moderate positive ΔQ, however, the eventual development of large-scale nonlinear finite-amplitude propagating disturbances with smaller propagation velocities appears to be a robust feature of the flow response over plane beach geometry with forcing of the type (2.13). Returning to the questions raised in the introduction, we note that for a considerable range of positive ΔQ, the flow response is dominated by finite-amplitude disturbances of one type or another that propagate alongshore. Although the observed behaviour at Duck, NC (Oltman-Shay *et al.* 1989; Dodd *et al.* 1992) might be interpreted as consistent with that found here for small positive ΔQ, conclusions involving direct comparisons of model results with the SUPERDUCK data set should await model studies with beach topography that includes sand bars. The results found here indicate for plane beaches the possible existence in the nearshore surf zone of propagating finite-amplitude disturbances associated with shear instabilities of alongshore currents with properties not directly related to results of linear theory.

Appendix A. Scaling of variables

Numerical solutions to (2.1) with forcing (2.13) are obtained in dimensional variables. The topography $h = 0.05x$ and the parameters $V_{SM} = 1$ m s^{-1}, $L = 90$ m, $h_0 = 4.5$ m, $L^{(x)} = 1000$ m, $\nu = 10$ m^4 s^{-1} are fixed. Sets of experiments are run with different values for the alongshore scale of the domain $L^{(y)}$. The bottom friction coefficient μ is varied within the sets of experiments. Dimensionless solutions may be recovered by transforming to the starred variables in (2.2). With the other parameters held constant, the variation of μ gives a set of experiments in dimensionless variables for different values of $Q = \mu L/(V_{SM} h_0) = 20\mu$, where Q varies linearly with μ (m s^{-1}). The relative scaling of the dimensional and non-dimensional variables remains similar through the set of experiments because the variation of μ is only reflected in the variation of Q and not in the scaling of the variables in (2.2) or in R^{-1}.

The non-dimensionalization (2.2) that leads to (2.3) involves choosing the characteristic velocity $V_{SM} = h_0 \mathscr{F}_0/(\rho_0 \mu)$, where $\mathscr{F}_0$ is a characteristic force. The dimensional experiments here with V_{SM} fixed and μ varied correspond to cases where the forcing $\mathscr{F}_0$ is varied also. Dimensional results for which $\mathscr{F}_0$ is fixed and μ is varied may of course be extracted from the present set of experiments transformed to dimensionless variables. The new dimensional variables, denoted by hats, are related to the starred dimensionless variables by

$$(\hat{x}, \hat{y}) = (x^\star, y^\star)L, \quad \hat{t} = t^\star L\mu\rho_0/(h_0\mathscr{F}_0), \qquad (A\ 1a,b)$$

$$(\hat{u}, \hat{v}) = (u^\star, v^\star)h_0\mathscr{F}_0/(\rho_0\mu), \quad \hat{h} = h^\star h_0, \qquad (A\ 1c,d)$$

and

$$Q = \mu^2 L\rho_0/(h_0^2\mathscr{F}_0), \quad R^{-1} = \nu\mu\rho_0/(h_0\mathscr{F}L^3). \qquad (A\ 2a,b)$$

In this case, Q varies as μ^2 and the scaling of the velocity components and the time variable both depend on μ and change as μ changes. The values of R^{-1} also vary with μ, but that should be unimportant in the limit $R^{-1} \ll 1$ (2.6).

Appendix B. Numerical methods

The numerical finite-difference approximations and the solution procedures for the shallow-water equations (2.1) are discussed in this appendix. To facilitate the presentation, the following operators

$$\delta_x\phi = \left[\phi(x + \tfrac{1}{2}\Delta x) - \phi(x - \tfrac{1}{2}\Delta x)\right]/\Delta x, \qquad (B\ 1a)$$

$$\overline{\phi}^x = \tfrac{1}{2}\left[\phi(x + \tfrac{1}{2}\Delta x) + \phi(x - \tfrac{1}{2}\Delta x)\right], \qquad (B\ 1b)$$

are defined for both the x- and y-directions. Also, we use the notation

$$\nabla^2\phi = (\delta_x^2 + \delta_y^2)\phi, \quad \overline{\phi}^{xy} = \overline{\overline{\phi}^x}^y. \qquad (B\ 1c,d)$$

The equations (2.1) are solved numerically by time stepping the momentum equations (2.1b,c). The pressure p is found from the solution to an elliptic equation that ensures the satisfaction of (2.1a). The finite-difference approximations are implemented on a C grid (Arakawa & Lamb 1977). The following centred second-order spatial difference scheme is utilized:

$$\delta_x[\overline{h}^x u] + \delta_y[\overline{h}^y v] = 0, \tag{B 2a}$$

$$(\overline{h}^x u)_t + \delta_x[h(\overline{u}^x)^2] + \delta_y[\overline{h}^{xy}\overline{u}^y\overline{v}^x] = -\overline{h}^x\delta_x p/\rho_0 - \mu u - \nu\overline{h}^x\nabla^4 u, \tag{B 2b}$$

$$(\overline{h}^y v)_t + \delta_x[(\overline{h}^{xy}\overline{v}^x\overline{u}^y] + \delta_y[h(\overline{v}^y)^2] = -\overline{h}^y\delta_y p/\rho_0 - \mu[v - V] - \nu\overline{h}^y\nabla^4 v. \tag{B 2c}$$

An equation for p is derived by combining δ_x(B2b) + δ_y(B2c) and using (B2a):

$$\rho_0^{-1}\left[\delta_x(\overline{h}^x\delta_x p) + \delta_y(\overline{h}^y\delta_y p)\right] = -\delta_x^2[h(\overline{u}^x)^2] - 2\delta_x\delta_y[\overline{h}^{xy}\overline{u}^y\overline{v}^x] - \delta_y^2[h(\overline{v}^y)^2]$$
$$- \mu[\delta_x u + \delta_y v - \delta_y V] - \nu[\delta_x(\overline{h}^x\nabla^4 u) + \delta_y(\overline{h}^y\nabla^4 v)]. \tag{B 3}$$

The boundary conditions (2.12),

$$u = u_{xx} = v_x = v_{xxx} = 0 \quad \text{at} \quad x = 0, L^{(x)}, \tag{B 4a--d}$$

are applied as follows. On a C grid, the variables u and v are defined at x and y values

$$u[i\Delta x, (j + \tfrac{1}{2})\Delta y, t], \quad i = 0, ..., N^{(x)}, \quad j = 1, ..., N^{(y)}, \tag{B 5a}$$

$$v[(i - \tfrac{1}{2})\Delta x, j\Delta y, t)], \quad i = 0, ..., N^{(x)} + 1, \quad j = 1, ..., N^{(y)}, \tag{B 5b}$$

where $N^{(x)} = L^{(x)}/\Delta x$, $N^{(y)} = L^{(y)}/\Delta y$, and where, for computational convenience in implementing (B4c,d), v is specified on exterior grid points at $x = -\tfrac{1}{2}\Delta x$ and $x = L^{(x)} + \tfrac{1}{2}\Delta x$. The boundary conditions (B4) are satisfied by setting

$$u(i\Delta x) = \nabla^2 u(i\Delta x) = 0, \tag{B 6a, b}$$

$$v[(i - \tfrac{1}{2})\Delta x] = v[(i + \tfrac{1}{2})\Delta x], \tag{B 6c}$$

$$\nabla^2 v[(i - \tfrac{1}{2})\Delta x] = \nabla^2 v[(i + \tfrac{1}{2})\Delta x], \quad \text{at} \quad i = 0, N^{(x)}. \tag{B 6d}$$

Correct boundary conditions for the pressure equation (B3) are applied naturally by deriving (B3) from (B2a,b,c) in finite-difference form with (B6) incorporated. In addition, to obtain a unique solution for p we require

$$\int_0^{L^{(y)}} \int_0^{L^{(x)}} p\,\mathrm{d}x\,\mathrm{d}y = 0. \tag{B 7}$$

For the time difference approximations, the time variable is discretized in the usual manner $t = n\Delta t$ where n is an integer and Δt is a constant time step. The notation $u^n = u(t = n\Delta t)$ is used to denote evaluation of u at time level n. We use the second-order Adams–Bashforth time difference scheme where, for example

$$u^{n+1} = u^n + \tfrac{1}{2}\Delta t(3u_t^n - u_t^{n-1}). \tag{B 8}$$

At general times with u, v, p known at level n and previous levels, u^{n+1} and v^{n+1} are found from the time difference scheme, and then p^{n+1} is found from the solution to

(B 3). At the initial time $t = 0, u^0$ and v^0 are specified consistent with (B 2a) and p^0 is found from (B 3). A forward step is used in place of (B 8) for $n = 0$.

For most of the numerical experiments, we use a uniform (x, y) grid with $\Delta x = \Delta y = 5$ m. The adequacy of this grid resolution is assessed in additional experiments with $n = 6$ and $L^{(y)} = 3(2\pi/k_0) = 540$ m by comparison of solutions obtained for $\mu = 0.011$, 0.006, and 0.003 with $\Delta x = \Delta y = 5$ m to those obtained using the same parameter values, but with the grid size reduced to $\Delta x = \Delta y = 2.5$ m. The same behaviour is found in the corresponding solutions, including the evolution of waves, growing initially at scale $2\pi/k_0$, into larger wavelength nonlinear disturbances (two disturbances develop for $\mu = 0.011$ and one for $\mu = 0.006$ and 0.003). The transitions occur in a similar manner at essentially the same times to larger wavelength disturbances with similar characteristics. Some quantitative differences exist, but these are not inconsistent with variations expected in unstable flow fields. We also investigated the effect of changing the relative phase of the cosine components in the perturbation forcing (2.13c). Experiments were run with $n = 3$, $L^{(y)} = 2(2\pi/k_0) = 900$ m, $\mu = 0.0055$, and with the phase θ_1 of the $\epsilon b_1 \cos\left[(2\pi y/L^{(y)}) + \theta_1\right]$ term varied so that $\theta_1 = \frac{1}{4}\pi, \frac{1}{2}\pi, \frac{3}{4}\pi$, where $\theta_1 = 0$ corresponds to the original experiment. Essentially the same behaviour is found. Qualitatively similar transitions from two waves to one wave result with some differences present in the details and timing of the transitions.

For calculation of the terms in the potential vorticity equations (5.2) and (2.21), we use $q'_\eta = q'_y$ and the approximations

$$\bar{v} = \frac{1}{N^{(y)}} \sum_{j=1}^{N^{(y)}} v(x, j\Delta y, t), \quad v' = v - \bar{v}, \tag{B 9a,b}$$

$$\bar{\zeta} = \delta_x \bar{v}, \quad \bar{q} = \bar{\zeta}/\bar{h}^{xy}, \quad \zeta' = \delta_x v' - \delta_y u', \quad q' = \zeta'/\bar{h}^{xy}, \tag{B 9c-f}$$

$$q'_s = -\Big\{\overline{u'}^y \delta_x \overline{q}^x + (\overline{v}^x - c)\delta_y \overline{q}^y + \overline{u'}^y \delta_x \overline{q'}^x + \overline{v'}^x \delta_y \overline{q'}^y - \overline{\overline{u'}^y \delta_x q'^x} - \overline{\overline{v'}^x \delta_y q'^y}$$

$$+ (\mu/\bar{h}^{xy})\big[\delta_x(v'/\bar{h}^y) - \delta_x(V'/\bar{h}^y) - \delta_y(u'/\bar{h}^x)\big] + (\nu/\bar{h}^{xy})\nabla^4\zeta'\Big\}, \tag{B 10}$$

where q'_s is obtained from the sum of the terms on the right-hand side of (B 10), and

$$\bar{q}_t = -\Big\{\overline{\overline{u'}^y \delta_x q'^x} + \overline{\overline{v'}^x \delta_y q'^y} + (\mu/\bar{h}^{xy})\delta_x\big[(\bar{v} - V_S)/\bar{h}^y\big] + (\mu/\bar{h}^{xy})\nabla^4\bar{\zeta}\Big\}, \tag{B 11}$$

where $\bar{q}_t$ is obtained from the sum of terms on the right-hand side of (B 11).

The spatial difference scheme in (B 10) involves centred second-order approximations to the terms in (5.2). It is not necessarily precisely equivalent to the finite-difference form of the potential vorticity equation derived in difference form from (B 2). Nevertheless, q'_s obtained from (B 10) is found to be extremely close to q'_s calculated from u' and v' after time stepping (B 2) with (B 8). This indicates that use of (B 10) is satisfactory for the evaluation of the balance of terms in (5.2) at any given time. Similar remarks apply to (B 11).

Finite-difference methods are also utilized to solve the linear stability problem (3.4). The variable $\phi(x)$ is defined at the same x grid points as u (B 5a) while $V_S(x)$ and $h(x)$ are defined at the same interior x points as v (B 5b). The following centred

second-order difference scheme is utilized for (3.4):

$$2\delta_x(V_S\delta_x\phi) - \delta_x^2(\phi\overline{V_S}^x) - k^2\overline{V_S}^x\phi - c\left[\delta_x^2\phi - \delta_x h\overline{\left(\frac{\delta_x\phi}{h}\right)}^x - k^2\phi\right]$$

$$+\delta_x h\left[\overline{\left(\frac{\delta_x(\phi\overline{V_S}^x)}{h}\right)}^x - 2\overline{\left(\frac{V_S\delta_x\phi}{h}\right)}^x + \frac{i\mu}{k}\overline{\left(\frac{\delta_x\phi}{h^2}\right)}^x\right] - \frac{i\mu}{k}\left[\delta_x\left(\frac{\delta_x\phi}{h}\right) - k^2\frac{\phi}{\overline{h}^x}\right] = 0.$$

$$\text{(B 12)}$$

Equation (B 12) is written so that the x finite-difference approximations are consistent with those implied by the derivation of (B 12) from the difference equations (B 2a,b,c) after linearization about $v = V_S(x)$. The boundary conditions (3.5) are

$$\phi(i\Delta x) = 0, \quad i = 0, N^{(x)}. \tag{B 13}$$

Equations (B 12) and (B 13) lead to a matrix equation,

$$A\phi = cB\phi, \tag{B 14}$$

where A and B are tridiagonal matrices. From (B14) we obtain

$$B^{-1}A\phi = c\phi, \tag{B 15}$$

which may be readily solved for the eigenvalues c and corresponding eigenvectors ϕ.

The grid resolution utilized is the same as in the numerical experiments, $\Delta x = 5$ m.

Appendix C. Lyapunov exponents, $n = 3$, $m = 1$

For $\mu \leqslant 0.0025$, the behaviour of solutions found in §4 from experiments with $n = 3$ and $L^{(y)} = 450$ m as represented in the (KE', EC) plane (figure 6) appears to be chaotic. We examine the possibility of verifying that impression and of quantifying to some extent the degree of chaos present in these solutions by calculation of the largest Lyapunov exponent. We utilize a procedure called the standard method (Bennettin, Galgani & Strelcyn 1976; Wolf *et al.* 1985; Goldhirsch, Sulem & Orszag 1987) applied to a system of partial differential equations (e.g. Sirovich & Deane 1991).

The following linearized equations for perturbations $(\tilde{u}, \tilde{v}, \tilde{p})$ about solutions (u, v, p) to (2.1) are used:

$$(h\tilde{u})_x + (h\tilde{v})_y = 0, \tag{C 1a}$$

$$(h\tilde{u})_t + 2(h\tilde{u}u)_x + (h\tilde{u}v)_y + (hu\tilde{v})_y = -h\tilde{p}_x/\rho_0 - r\tilde{u} - \nu\nabla^4\tilde{u}, \tag{C 1b}$$

$$(h\tilde{v})_t + (h\tilde{u}v)_x + (hu\tilde{v})_x + 2(h\tilde{v}v)_y = -h\tilde{p}_y/\rho_0 - r\tilde{v} - \nu\nabla^4\tilde{v}. \tag{C 1c}$$

The norm is based on area-averaged kinetic energy,

$$\widetilde{KE} = \tfrac{1}{2}\{h(\overline{\tilde{u}^2} + \overline{\tilde{v}^2})\}. \tag{C 2}$$

Solutions of (C 1) for $(\tilde{u}, \tilde{v}, \tilde{p})$ are calculated simultaneously with the calculation of solutions of (2.1) for (u, v, p). The initial conditions for $(\tilde{u}, \tilde{v})$ at $t = t_0$ are arbitrary. We take

$$\tilde{u} = 0, \quad \tilde{v} = 0.01\ V_S(x) \quad \text{at} \quad t = t_0. \tag{C 3a,b}$$

The variables $(\tilde{u}, \tilde{v}, \tilde{p})$ are rescaled to reduce their magnitudes at times when $\widetilde{KE}$ has increased so that $\widetilde{KE} \geqslant 5.5$ m^3 s^{-2}.
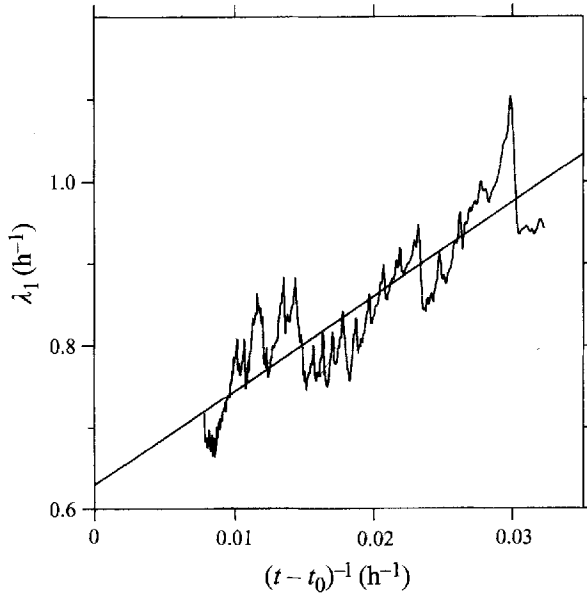
FIGURE 18. The calculated value of $\lambda_1(t)$ in (C4b) as a function of $(t - t_0)^{-1}$ for the time period 40–137 h from the experiment with $\mu = 0.001$ m s^{-1} ($n = 3$, $L^{(y)} = 450$ m). The linear regression line is also shown.

The largest Lyapunov exponent in the kinetic energy norm (C2) is given by

$$\lambda_{1L} = \lim_{t \to \infty} \lambda_1(t), \qquad (C\ 4a)$$

$$\lambda_1(t) = \frac{1}{(t - t_0)} \left\{ \ln\left(\frac{\widetilde{KE}(t)}{\widetilde{KE}'(t_m)}\right) + \sum_{j=0}^{m-1} \ln\left(\frac{\widetilde{KE}(t_{j+1})}{\widetilde{KE}'(t_j)}\right) \right\}, \qquad (C\ 4b)$$

where t_0 is the initial time, t_j are the times when $(\tilde{u}, \tilde{v}, \tilde{p})$ are rescaled, t_m is the time of the last rescaling, $t > t_m \geqslant t_0$, and $\widetilde{KE}'(t_j)$ are the rescaled values of $\widetilde{KE}(t_j)$ (except that $\widetilde{KE}'(t_0) = \widetilde{KE}(t_0)$). Goldhirsch *et al.* (1987) have shown for n-dimensional dynamical systems that

$$\lambda_1(t) \sim \lambda_{1L} + (t - t_0)^{-1}\left[b_1 + \xi_1(t)\right] \quad \text{as} \quad t \to \infty, \qquad (C\ 5)$$

where b_1 is a constant and $\xi_1(t)$ is a noise term. We find that the calculated values of $\lambda_1(t)$ have behaviour consistent with (C5) and thus we utilize (C5) to obtain estimates for λ_{1L}.

Calculated values of $\lambda_1(t)$ for the experiment with $\mu = 0.001$ are shown in figure 18. The calculation of $(\tilde{u}, \tilde{v}, \tilde{p})$ is started at $t_0 = 9$ h, after initial transient adjustments in (u, v, p) have taken place (figure 3), and continued to $t = 137$ h. In figure 18, λ_1 is plotted as a function of $(t - t_0)^{-1}$ for the time period 40–137 h during which the asymptotic behaviour (C5) is observed. Based on (C5), an estimate $(\hat{\lambda}_{1L})$ for λ_{1L} is obtained by linear regression of $\lambda_1(t)$ on $(t - t_0)^{-1}$ during this time period. That least-squares straight-line fit is also plotted in figure 18 and the zero intercept gives $\hat{\lambda}_{1L} = 0.630 \pm 0.024$ h^{-1}. The positive value of $\hat{\lambda}_{1L}$ indicates that the solution for $\mu = 0.001$ is indeed chaotic. The implied time scale is $\hat{\lambda}_{1L}^{-1} \simeq 1.59$ h.

Similar slow convergence of $\lambda_1(t)$ was found in additional experiments at other values of μ. Although the observed tendency was always toward $\hat{\lambda}_{1L} > 0$ for the

visually irregular solutions and toward $\hat{\lambda}_{1L} \simeq 0$ for the limit cycles, the calculations were not carried out to large enough times to obtain good estimates of λ_{1L}. It is clear that this procedure could be consistently applied to all the experiments in this set with different values of μ. However, because of the large computation times required to do so and the secondary nature of these results, it was decided not to pursue that aspect of the problem further in this study.

REFERENCES

ARAKAWA, A. & LAMB, V. R. 1977 Computational design of the basic dynamical processes of the UCLA general circulation model. *Meth. Comput. Phys,* **17**, 173–265.

ARNEODO, A., COULLET, P., TRESSER, C., LIBCHABER, A., MAURER, J. & D'HUMIÈRES, D. 1983 On the observation of an uncompleted cascade in a Raleigh-Bénard experiment. *Physica* **6D**, 385–392.

BENNETTIN, G., GALGANI, L. & STRELCYN, J.-M. 1976 Kolmogorov entropy and numerical experiments. *Phys. Rev. A* **14**, 2338–2345.

BOWEN, A. J. & HOLMAN, R. A. 1989 Shear instabilities of the mean longshore current, 1. Theory. *J. Geophys. Res.* **94**(C12), 18023–18030.

DEIGAARD, R., CHRISTENSEN, E. D., DAMGAARD, J. S. & FREDSØE, J. 1994 Numerical simulation of finite amplitude shear waves and sediment transport. *Proc. 24th Intl Conf. Coastal Engng,* pp. 1919–1933. ASCE.

DODD, N. 1994 On the destabilization of a longshore current on a plane beach: Bottom shear stress, critical conditions, and onset of instability, *J. Geophys. Res.* **99**(C1), 811–828.

DODD, N., OLTMAN-SHAY, J. & THORNTON, E. B. 1992 Shear instabilities in the longshore current: A comparison of observation and theory. *J. Phys. Oceanogr.* **22**, 62–82.

DODD, N. & THORNTON, E. B. 1990 Growth and energetics of shear waves in the nearshore. *J. Geophys. Res.* **95**(C9), 16075–16083.

DODD, N. & THORNTON, E. B. 1992 Longshore current instabilities: growth to finite amplitude. *Proc. 23rd Intl. Conf. Coastal Engng,* pp. 2655–2668. ASCE.

DRAZIN, P. G. & REID, W. H. 1981 *Hydrodynamic Stability* Cambridge University Press.

FALQUÉS, A. & IRANZO, V. 1994 Numerical simulation of vorticity waves in the nearshore. *J. Geophys. Res.* **99**(C1), 825–841.

FALQUÉS, A., IRANZO, V. & CABALLERIA, M. 1994 Shear instability of longshore currents: effects of dissipation and non-linearity. *Proc. 24th Intl Conf. Coastal Engng,* pp. 1983–1997. ASCE.

GOLDHIRSCH, I., SULEM, P-L. & ORSZAG, S. A. 1987 Stability and Lyapunov stability of dynamical systems: A differential approach and a numerical method. *Physica* **27D**, 311–337.

FEIGENBAUM, M. J. 1978. Quantitative universality for a class of nonlinear transformations. *J. Statist. Phys.* **19**, 25–52.

FEIGENBAUM, M. J. 1983 Universal behaviour in nonlinear systems. *Physica* **7D**, 16–39.

HO, C.-M. & HUERRE, P. 1984 Perturbed free shear layers. *Ann Rev. Fluid Mech.* **16**, 365–424.

KLAASSEN, G. P. & PELTIER, W. R. 1989 The role of transverse secondary instabilities in the evolution of free shear layers. *J. Fluid Mech.* **202**, 367–402.

LIBCHABER, A. & MAURER, J. 1982 A Rayleigh-Bénard experiment: helium in a small box. In *Nonlinear Phenomena at Phase Transitions and Instabilities* (ed. T. Riste), pp. 259–286. Plenum.

OLTMAN-SHAY, J., HOWD, P. A. & BIRKEMEIER, W. A. 1989 Shear instabilities of the mean longshore current, 2. Field data. *J. Geophys. Res.* **94**(C12), 18031–18042.

SIROVICH, L. & DEANE, A. E. 1991. A computational study of Rayleigh-Bénard convection. Part 2. Dimension considerations. *J. Fluid Mech.* **222**, 251–265.

WOLF, A., SWIFT, J. B., SWINNEY, H. L. & VASTANO, J. A. 1985 Determining Lyapunov exponents from a time series. *Physica* **16D**, 285–317.